

On the modelling, linear stability, and numerical simulation for advection-diffusion-reaction in poroelastic media

Nitesh Verma^a, Bryan Gómez-Vargas^{b,c}, Luis Miguel De Oliveira Vilaca^d, Sarvesh Kumar^a, Ricardo Ruiz-Baier^{e,*}

^aDepartment of Mathematics, Indian Institute of Space Science and Technology, Trivandrum 695 547, India.

^bCI²MA and Departamento de Ingeniería Matemática, Universidad de Concepción, Casilla 160-C, Concepción, Chile.

^cSección de Matemática, Sede de Occidente, Universidad de Costa Rica, San Ramón, Alajuela, Costa Rica.

^dLaboratory of Artificial & Natural Evolution (LANE), Department of Genetics and Evolution, University of Geneva, 4 Boulevard d'Yvroy, 1205 Geneva, Switzerland.

^eMathematical Institute, University of Oxford, A. Wiles Building, Woodstock Road, Oxford OX2 6GG, UK.

Abstract

We perform the linear growth analysis for a new PDE-based model for poromechanical processes (formulated in mixed form using the solid deformation, fluid pressure, and total pressure) interacting with diffusing and reacting solutes in the medium. We find parameter regions that lead to interesting behaviour of the coupled system. These mutual dependences between deformation and diffusive patterns are of substantial relevance in the study of morphoelastic changes in biomaterials. We provide a set of computational examples in 2D and 3D that can be used to form a better understanding on how, and up to which extent, the deformations of the porous structure dictate the generation and suppression of spatial patterning dynamics, also related to the onset of mechano-chemical waves.

Keywords: Biot equations, reaction-diffusion, nonlinear coupling, linear stability analysis, mixed finite elements, numerical examples.

2000 MSC: 65M60, 74F10, 35K57, 74L15.

1. Introduction

We propose a new model for the interaction between diffusing species and an underlying poroelastic structure. This work is composed by two main contributions. In [49] we have recently explored the well-posedness of the coupled system and have addressed the stability of a mixed finite element discretisation. On the other hand, in the present companion paper we focus more on the modelling issues, on the spectral linear stability analysis, and we also provide numerical examples dealing with growth and pattern formation, as well as with applications in traumatic brain injury.

As considered here, reaction-diffusion equations are coupled to the balances of mass and linear momentum of the fluid-solid mixture through advection, and though a modification in the reaction

*Author for correspondence. Email: ruizbaier@maths.ox.ac.uk. Phone: +44 1865 615168.

Email addresses: nitesh@iist.ac.in (Nitesh Verma), bgomez@ci2ma.udec.cl (Bryan Gómez-Vargas), LuisMiguel.DeOliveiraVilaca@unige.ch (Luis Miguel De Oliveira Vilaca), sarvesh@iist.ac.in (Sarvesh Kumar), ruizbaier@maths.ox.ac.uk (Ricardo Ruiz-Baier)

Funding: This work has been partially supported by CONICYT through the Becas-Chile Programme for foreign students, and by the London Mathematical Society through Scheme 5, Grant 51703.

modulated by changes in volume. In turn, the solutes and the external forces drive the motion of the medium through contractile forces. Even if the present theoretical framework is motivated by examples in cell dynamics, applications sharing the same mathematical and mechano-chemical structure are numerous. These include the formation of inflammatory edema in the context of immune systems [38], oxygen diffusivity in cartilage [25], contaminant transport [4], petroleum extraction [7], drug transport in arteries [8], rock consolidation and fractures [33], tumour localisation and biomass growth [41], or chemically-controlled cell motion [26]. In some of these phenomena, one can observe mechanically-induced transport of the solutes. This effect occurs as the consolidation of the porous media increases the flow of interstitial fluid which in turn contributes to the solute advective transport (see e.g. [40]). On the other hand, the presence of chemical solutes in so-called active poroelastic materials locally modifies morphoelastic properties [36], and these processes can be homogenised to obtain macroscopic models of poroelasticity coupled with advection-reaction-diffusion equations (see e.g. [10, 32]).

Very often, these coupled models are of high-dimensions and very nonlinear, which impedes to obtain exact solutions in closed form. Even if a large variety of numerical methods exist for producing approximate solutions, appropriate methods (in the sense of being robust with respect to model parameters, being convergent, and replicating key properties of the underlying physico-chemical phenomena) have appeared only recently. Modern techniques include [23], where the authors propose mixed finite element schemes and provide a stability analysis for a system of multiple-network poroelasticity, that resembles the model problem we are interested in. As in [23], here we also employ the mixed three-field formulation for poroelasticity from [31, 22], and in [49] we develop the coupling with a primal formulation for the advection-diffusion system.

Beyond the question of the equations' resolution, enhancement of the complexity of the models leads the stability analysis to become more and more analytically involved. Stability analysis enables to understand and to anticipate partially the essential physical mechanisms of the proposed system with respect to the parameter values. Such tool is particularly useful in the context of patterning systems to locate the parameter space where the model leads to stationary spatially unstable solutions. In the context of the present work, related studies have been performed on particular sub-systems such as reaction-diffusion [13, 43] or decoupled elasticity and diffusion [28, 27]. More recent works tend to integrate further complexity in the model by taking care of multi-layered coupled systems [9], incorporating domain or mechanical growth [11, 19], the coupling between elasticity-diffusion [12], poroelasticity [34, 37, 35], and also poroelasticity-diffusion [36], which resembles more the development we advocate in this work.

The remainder of this paper is laid out as follows. The governing equations proposed in [49] are recalled in Section 2. Then, in Section 3 we perform a linear stability analysis around a steady state with zero solid displacement, constant fluid pressure, and constant solute concentrations. To make the analysis as general as possible, we modify the momentum equilibrium that we presented in [49], now including also an acceleration term. We use that to make some model comparisons. We obtain dispersion relations that indicate that the mechano-chemical feedback onsets Turing instabilities (with non-trivial wavenumber) for a range of coupling parameters. We proceed in Section 4 with recalling the locking-free finite element scheme from the companion paper [49]. Then we give some illustrative numerical examples in 2D and 3D collected in Section 5, and we close in Section 6 with a discussion and concluding remarks.

2. Model problem

2.1. Poroelasticity of soft tissue

Let us consider flow of interstitial fluid through a porous medium that is subject to elastic deformations. We will consider that the process occurs in either two- or three-dimensional domains $\Omega \subset \mathbb{R}^d$

with $d \in \{2, 3\}$, and that the fluid does not enter nor leaves the body. As common in the study of flow in porous media, we adopt a description in terms of locally averaged variables. Then, for a given time $t \in (0, t_{\text{final}}]$, poromechanical quantities of interest are in this case the average displacement of the porous structure $\mathbf{u}^s(t) : \Omega \rightarrow \mathbb{R}^d$ and the pressure head associated with the fluid flowing through the pores, $p^f(t) : \Omega \rightarrow \mathbb{R}$. We also suppose that gravitational forces have little effect in contributing to the force balances in comparison to other external body forces such as applied loads depending on space and time variables $\mathbf{b}(t) : \Omega \rightarrow \mathbb{R}^d$. In the classical theory of consolidation as exposed in the seminal works [6, 47], the system allows to describe physical loading of porous layers and the change of hydraulic equilibrium in a fluid-structure system. There, one assumes as well that the exerted stresses contain shear contributions by the solid phase whereas volumetric contributions appear from both solid and the fluid phases (since the interstitial flow is considered governed by Darcy's law). This fact motivates the idea from [31, 22] to introduce an auxiliary scalar unknown

$$\psi = \alpha p^f - \lambda \operatorname{div} \mathbf{u}^s, \quad (2.1)$$

representing the total pressure, or the volumetric part of the total Cauchy stress $\boldsymbol{\sigma}$ (specified in the constitutive equation (2.3), below), where α is the so-called Biot-Willis consolidation (or pressure storage coupling) parameter.

Denoting by $\ell(t) : \Omega \rightarrow \mathbb{R}$ a given volumetric fluid source or sink, the conservation of total pore fluid content can be stated as an equation for the fluid pressure $p^f(t) : \Omega \rightarrow \mathbb{R}$

$$\left(c_0 + \frac{\alpha^2}{\lambda}\right) \partial_t p^f - \frac{\alpha}{\lambda} \partial_t \psi - \frac{1}{\eta} \operatorname{div}(\kappa \nabla p^f) = \ell, \quad (2.2)$$

where $\kappa(\mathbf{x})$ is the permeability (or hydraulic conductivity) of the porous medium which can possibly be anisotropic, η is the constant viscosity of the pore fluid, and c_0 is the constrained specific storage coefficient (which encompasses both the porosity of the solid skeleton and the compressibility of the fluid or of the solid in the meso-scale) [44].

The equations of motion (balance of linear momentum and the constitutive equation relating stress and strains) consist in finding solid displacements $\mathbf{u}^s(t) : \Omega \rightarrow \mathbb{R}^d$ such that

$$\boldsymbol{\sigma} = 2\mu \boldsymbol{\varepsilon}(\mathbf{u}^s) - \psi \mathbf{I}, \quad (2.3)$$

$$\rho \partial_{tt} \mathbf{u} - \operatorname{div} \boldsymbol{\sigma} = \rho \mathbf{b}, \quad (2.4)$$

where the total pressure is defined in (2.1), $\boldsymbol{\varepsilon}(\mathbf{u}) = \frac{1}{2}(\nabla \mathbf{u} + \nabla \mathbf{u}^T)$ is the tensor of infinitesimal strains, \mathbf{I} is the identity tensor, ρ denotes is the density of the saturated porous material, and μ, λ are the shear and dilation moduli associated with the constitutive law of the solid structure. These and all other model parameters are assumed positive and bounded, except for the dilation modulus λ , which approaches infinity for fully incompressible materials. In [49] we did not consider an acceleration term in the equation of balance of linear momentum (2.4) as one typically supposes that solid deformations are much slower than the fluid flow rate. Nevertheless we keep that term here, as we will also explore the influence of inertial effects in the context of linear stability analysis.

Recent applications of such consolidation theory to the poromechanical characterisation of soft living tissues confined to the regime of infinitesimal strains include mainly the formation and development of brain oedema [48, 38] and the importance of including pia matter [45], as well as periodontal layer and tooth interfaces [3]. On the other hand, extensions to large poromechanical deformations and finite growth have been devoted to ventilation processes in the lung parenchyma [5], early stages of feather primordia formation [15], pathological skin expansion [51], or morphoelasticity of arteries [46].

Using poroelasticity to model soft tissues is of high relevance since the permeability of tissue constituents such as collagenous membranes is typically in the orders of 10^{-14} to 10^{-12} [$\text{m}^2 \text{N}^{-1} \text{s}^{-1}$]. If one

considers membranes having a thickness of a few hundred microns, then fluid exchange occurs in the range of seconds and therefore this flow can perfectly affect physiological tissue deformations due to cardiac cycle or breathing [16]. Thus we will work under the assumption that a compound of living cells forms a macroscopic linear poroelastic structure fully saturated with interstitial fluid, and that its motion can be described by (2.1)-(2.4).

2.2. Macroscopic description of two-species motion

Next we turn to the incorporation of two interacting species whose dynamics occurs only by diffusion and reaction. These can represent many different systems, for instance bacteria and neutrophils as in [38], or two different morphogens as in [15]. In any case, the interaction between the diffusive solutes is modelled by a PDE system that includes reaction-diffusion, as well as advection by the velocity of the moving domain. Alternatively, one could also suppose that the species are advected only by the fluid velocity (or by the filtration velocity). Simpler models are able to take advantage of one-dimensional geometries, or of a constant material density of the constituents (e.g. cells) in order to obtain closed-form expressions for the advecting velocity [30]. Here we use the transient form of the equations of motion (2.4),(2.3) to determine such velocity.

We therefore consider the propagation of a generic species with concentration w_1 , reacting with an additional species with concentration w_2 . The problem can be written as follows

$$\partial_t w_1 + \partial_t \mathbf{u}^s \cdot \nabla w_1 - \operatorname{div}\{D_1(\mathbf{x}) \nabla w_1\} = f(w_1, w_2, \mathbf{u}^s), \quad (2.5)$$

$$\partial_t w_2 + \partial_t \mathbf{u}^s \cdot \nabla w_2 - \operatorname{div}\{D_2(\mathbf{x}) \nabla w_2\} = g(w_1, w_2, \mathbf{u}^s), \quad (2.6)$$

where D_1, D_2 are positive definite matrices containing possibly anisotropy of self-diffusion. The net reaction terms depend on parameters that account for the reproduction of species, the removal of species concentration due to reactive interactions, and the intrinsic changes due to local modifications in volume (that is, how the pore microstructure evolves with deformation). For illustrative purposes, and as in [49, 30], we can simply consider hypothetical kinetic specifications, which can also simplify the exposition of the linear stability analysis of Section 3. We choose a modification to the classical Schnackenberg model [42]

$$\begin{aligned} f(w_1, w_2, \mathbf{u}^s) &= \beta_1(\beta_2 - w_1 + w_1^2 w_2) + \gamma w_1 \partial_t \operatorname{div} \mathbf{u}^s, \\ g(w_1, w_2, \mathbf{u}^s) &= \beta_1(\beta_3 - w_1^2 w_2) + \gamma w_2 \partial_t \operatorname{div} \mathbf{u}^s, \end{aligned}$$

where $\beta_1, \beta_2, \beta_3, \gamma$ are positive rate constants. As mentioned above, the mechano-chemical feedback operates only by advection and the last two terms defining f, g . These terms are modulated by $\gamma > 0$, and therefore they act as a local source for a given species if the solid volume increases, otherwise the additional terms contribute to removal of species concentration [30].

2.3. Active stress

We assume that stresses are exerted by solid, by fluid, and by morphogens. Then the forces are condensed in a macroscopic balance equation for the mixture where we recall that the solid phase is simply considered as an isotropic deformable porous medium and that the fluid phase only contributes volumetrically to the stress through the hydrostatic fluid pressure at the interstitium. Microscopic tension generation is here supposed to occur due to active stresses (2.3) and

$$\boldsymbol{\sigma}_{\text{total}} = \boldsymbol{\sigma} + \boldsymbol{\sigma}_{\text{act}}, \quad (2.7)$$

where the active stress operates primarily on a given, constant direction \mathbf{k} , and its intensity depends on a scalar field $r = r(w_1, w_2)$ and on a positive constant τ , to be specified later on (see e.g. [20])

$$\boldsymbol{\sigma}_{\text{act}} = -\tau r \mathbf{k} \otimes \mathbf{k}. \quad (2.8)$$

2.4. Initial and boundary conditions under different model configurations

We employ appropriate initial data at rest

$$w_1(0) = w_{1,0}, \quad w_2(0) = w_{2,0}, \quad \mathbf{u}^s(0) = \mathbf{0}, \quad \partial_t \mathbf{u}^s(0) = \mathbf{0}, \quad p^f(0) = 0, \quad \psi(0) = 0 \quad \text{in } \Omega \times \{0\}.$$

Regarding boundary conditions, the species concentrations will assume zero diffusive flux boundary conditions on the whole boundary

$$D_1(\mathbf{x}) \nabla w_1 \cdot \mathbf{n} = 0 \quad \text{and} \quad D_2(\mathbf{x}) \nabla w_2 \cdot \mathbf{n} = 0 \quad \text{on } \partial\Omega \times (0, t_{\text{final}}].$$

For the poromechanics we adopt either Robin conditions for the deformations (mimicking the presence of supporting springs) and zero fluid flux everywhere on the boundary,

$$[2\mu\boldsymbol{\varepsilon}(\mathbf{u}^s) - \psi \mathbf{I} + \boldsymbol{\sigma}_{\text{act}}] \mathbf{n} + \zeta \mathbf{u}^s = \mathbf{0} \quad \text{and} \quad \frac{\kappa}{\eta} \nabla p^f \cdot \mathbf{n} = 0 \quad \text{on } \partial\Omega \times (0, t_{\text{final}}], \quad (2.9)$$

where $\zeta > 0$ is the (possibly time-dependent) stiffness of the spring; or as in [49] we can separate the boundary $\partial\Omega = \Gamma \cup \Sigma$ into two parts Γ and Σ where we prescribe clamped boundaries and zero fluid normal fluxes; and zero (total) traction together with constant fluid pressure, respectively

$$\mathbf{u}^s = \mathbf{0} \quad \text{and} \quad \frac{\kappa}{\eta} \nabla p^f \cdot \mathbf{n} = 0 \quad \text{on } \Gamma \times (0, t_{\text{final}}], \quad (2.10)$$

$$[2\mu\boldsymbol{\varepsilon}(\mathbf{u}^s) - \psi \mathbf{I} + \boldsymbol{\sigma}_{\text{act}}] \mathbf{n} = \mathbf{0} \quad \text{and} \quad p^f = 0 \quad \text{on } \Sigma \times (0, t_{\text{final}}]. \quad (2.11)$$

Each case will be specified in the tests of Sections 3 and 5.

3. Linear stability analysis and dispersion relation

Next we proceed to derive a linear stability analysis similarly as done in [30]. This analysis delivers insight regarding the interaction mechanisms between tissue deformation and diffusing solutes. Our development is however more general and more involved, since we are including acceleration effects in the momentum equilibrium equation. We skip as much as possible the lengthy details of the derivation, and concentrate only in the dispersion relation. Note that since the functions f and g are prescribed, we can specify a steady state given by $w_1 = w_{1,0} = \beta_2 + \beta_3$, $w_2 = w_{2,0} = \frac{\beta_3}{(\beta_2 + \beta_3)^2}$, $p = p_0$, $\psi = \psi_0$ and $\mathbf{u} = \mathbf{0}$.

Linear stability analysis revolves on the study of the eigenvalue-eigenvector systems evaluated from the linearisation of the coupled PDE around their steady state [43]. This tool enables to understand more deeply the behaviour (stability) of the linearised system with respect to certain types of perturbations around the steady state. The main idea is to postulate a solution of the linearised system, being of the form $\Phi \exp(i\mathbf{k} \cdot \mathbf{x} + \phi t)$, where Φ is a constant eigenvector of size equal to number of independent variables in our model (e.g., here $4 + d$ for \mathbb{R}^d), while ϕ is the eigenvalue, also called linear growth factor, that is directly linked to the stability of our system. The term \mathbf{k} (resp. $k = |\mathbf{k}|$) is the wave vector (resp. wave number) that is a measure of the spatial structure of our eigen-solution. Depending on the boundary conditions applied to our model, the value of k is bounded and delimited by the geometry of our domain and the constraint that the eigen-solution must satisfy the boundary conditions. To avoid additional complexity, we centre our analysis on an infinite domain in \mathbb{R}^d , with $d = \{2, 3\}$.

3.1. General form of the dispersion relation

Following e.g. [50], we can derive a dispersion relation that is eventually defined by the product of two distinct polynomials

$$P(\phi; k^2) = P_1(\phi; k^2)^{d-1} P_2(\phi; k^2),$$

where $P_1(\phi; k^2) = \rho\phi^2 + \mu k^2$, and where $d = \{2, 3\}$ is the spatial dimension of the infinite domain $\Omega = \mathbb{R}^d$, where the linear stability analysis of the coupled problem (2.2)-(2.4) is performed.

Since P_1 is a polynomial with pure imaginary roots, it does not have an influence on the stability of the steady state version of (2.2)-(2.4). Consequently, we can focus our attention on P_2 which is a fifth-order polynomial given by

$$P_2(\phi; k^2) = A_5(k^2)\phi^5 + A_4(k^2)\phi^4 + A_3(k^2)\phi^3 + A_2(k^2)\phi^2 + A_1(k^2)\phi + A_0(k^2), \quad (3.1)$$

where

$$\begin{aligned} A_5(k^2) &= \rho c_0, \\ A_4(k^2) &= \rho \left(c_0(D_1 + D_2) + \frac{\kappa}{\eta} \right) k^2 - \rho c_0 \beta_1 \frac{\beta_3 - \beta_2 - (\beta_2 + \beta_3)^3}{\beta_2 + \beta_3}, \\ A_3(k^2) &= \rho \left(\frac{\kappa}{\eta} (D_1 + D_2) + c_0 D_1 D_2 \right) k^4 \\ &\quad + \left[c_0(2\mu + \lambda) + \alpha^2 - \rho c_0 \beta_1 \frac{D_2(\beta_3 - \beta_2) - D_1(\beta_2 + \beta_3)^3}{\beta_2 + \beta_3} - \frac{\kappa \rho}{\eta} \beta_1 \frac{\beta_3 - \beta_2 - (\beta_2 + \beta_3)^3}{\beta_2 + \beta_3} \right] k^2 \\ &\quad + \rho c_0 \beta_1^2 (\beta_2 + \beta_3)^2 - i\gamma \left[\sum_{j=1}^d \hat{\Upsilon}_j k_j \right] c_0 (w_{1,0} \theta_1 + w_{2,0} \theta_2), \\ A_2(k^2) &= \frac{\kappa \rho}{\eta} D_1 D_2 k^6 + \left[(c_0(2\mu + \lambda) + \alpha^2) (D_1 + D_2) + \frac{\kappa}{\eta} (2\mu + \lambda) - \frac{\kappa \rho}{\eta} \beta_1 \frac{D_2(\beta_3 - \beta_2) - D_1(\beta_2 + \beta_3)^3}{\beta_2 + \beta_3} \right] k^4 \\ &\quad + \left[\frac{\kappa \rho}{\eta} \beta_1^2 (\beta_2 + \beta_3)^2 - (c_0(2\mu + \lambda) + \alpha^2) \beta_1 \frac{\beta_3 - \beta_2 - (\beta_2 + \beta_3)^3}{\beta_2 + \beta_3} \right] k^2 \\ &\quad - i\gamma \left[\sum_{j=1}^d \hat{\Upsilon}_j k_j \right] \left[\left(\frac{\kappa}{\eta} (w_{1,0} \theta_1 + w_{2,0} \theta_2) + c_0 (w_{1,0} \theta_1 D_2 + w_{2,0} \theta_2 D_1) \right) k^2 \right. \\ &\quad \left. + c_0 \left(-w_{1,0} \theta_2 \frac{2\beta_1 \beta_3}{\beta_2 + \beta_3} + w_{2,0} \theta_1 \beta_1 (\beta_2 + \beta_3)^2 + w_{1,0} \theta_1 \beta_1 (\beta_2 + \beta_3)^2 - w_{2,0} \theta_2 \frac{\beta_1 (\beta_3 - \beta_2)}{\beta_2 + \beta_3} \right) \right], \\ A_1(k^2) &= \left[\frac{\kappa}{\eta} (2\mu + \lambda) (D_1 + D_2) + (c_0(2\mu + \lambda) + \alpha^2) D_1 D_2 \right] k^6 \\ &\quad - \left[(c_0(2\mu + \lambda) + \alpha^2) \beta_1 \frac{D_2(\beta_3 - \beta_2) - D_1(\beta_2 + \beta_3)^3}{\beta_2 + \beta_3} + \frac{\kappa}{\eta} (2\mu + \lambda) \beta_1 \frac{\beta_3 - \beta_2 - (\beta_2 + \beta_3)^3}{\beta_2 + \beta_3} \right] k^4 \\ &\quad + (c_0(2\mu + \lambda) + \alpha^2) \beta_1^2 (\beta_2 + \beta_3)^2 k^2 - i \frac{\kappa \gamma}{\eta} \left[\sum_{j=1}^d \hat{\Upsilon}_j k_j \right] \left[(w_{1,0} \theta_1 D_2 + w_{2,0} \theta_2 D_1) k^2 \right. \\ &\quad \left. - w_{1,0} \theta_2 \frac{2\beta_1 \beta_3}{\beta_2 + \beta_3} + w_{2,0} \theta_1 \beta_1 (\beta_2 + \beta_3)^2 + w_{1,0} \theta_1 \beta_1 (\beta_2 + \beta_3)^2 - w_{2,0} \theta_2 \frac{\beta_1 (\beta_3 - \beta_2)}{\beta_2 + \beta_3} \right] k^2, \\ A_0(k^2) &= \frac{\kappa}{\eta} (2\mu + \lambda) k^4 \left(D_1 D_2 k^4 - \beta_1 \frac{D_2(\beta_3 - \beta_2) - D_1(\beta_2 + \beta_3)^3}{\beta_2 + \beta_3} k^2 + \beta_1^2 (\beta_2 + \beta_3)^2 \right), \end{aligned}$$

where the coefficients $w_{j,0}$, for $j = \{1, 2\}$, are the steady state concentrations of generic species w_j , and $\theta_j = (\partial_{\mathbf{w}} \sigma_{act}(\mathbf{w}_0))_j$ with $\sigma_{act}(\mathbf{w}) = -\tau r(\mathbf{w})$; $\hat{\Upsilon}_j = \Upsilon_{\cdot j} + i \tilde{\Upsilon}_j$, with $\Upsilon_{\cdot j} = \sum_k \partial_{\mathbf{x}_k} \Upsilon_{kj}$, $\tilde{\Upsilon}_j = \sum_k k_k \Upsilon_{kj}$ and $\Upsilon = \mathbf{k} \otimes \mathbf{k}$.

For the rest of the linear analysis, we impose that $\Upsilon = \mathbf{I}$, with \mathbf{I} the identity matrix, $r^{(1)}(\mathbf{w}) = w_1 + w_2$, $r^{(2)}(\mathbf{w}) = w_1^2$ and $\mathbf{b} = \mathbf{0}$. In such condition, only the coefficients A_3, A_2, A_1 are modified and they adopt the following forms

$$A_3(k^2) = \left[\rho \left(\frac{\kappa}{\eta} (D_1 + D_2) + c_0 D_1 D_2 \right) \right] k^4$$

$$\begin{aligned}
& + \left[c_0(2\mu + \lambda) + \alpha^2 - \rho c_0 \beta_1 \frac{D_2(\beta_3 - \beta_2) - D_1(\beta_2 + \beta_3)^3}{\beta_2 + \beta_3} - \frac{\kappa \rho}{\eta} \beta_1 \frac{\beta_3 - \beta_2 - (\beta_2 + \beta_3)^3}{\beta_2 + \beta_3} \right. \\
& \quad \left. + \gamma c_0 \left((\beta_2 + \beta_3) \theta_1^{(i)} + \frac{\beta_3}{(\beta_2 + \beta_3)^2} \theta_2^{(i)} \right) \right] k^2 + \rho c_0 \beta_1^2 (\beta_2 + \beta_3)^2, \\
A_2(k^2) &= \frac{\kappa \rho}{\eta} D_1 D_2 k^6 + \left[(c_0(2\mu + \lambda) + \alpha^2) (D_1 + D_2) + \frac{\kappa}{\eta} (2\mu + \lambda) - \frac{\kappa \rho}{\eta} \beta_1 \frac{D_2(\beta_3 - \beta_2) - D_1(\beta_2 + \beta_3)^3}{\beta_2 + \beta_3} \right. \\
& \quad \left. + \gamma \left(\frac{\kappa}{\eta} \left((\beta_2 + \beta_3) \theta_1^{(i)} + \frac{\beta_3}{(\beta_2 + \beta_3)^2} \theta_2^{(i)} \right) + c_0 \left((\beta_2 + \beta_3) \theta_1^{(i)} D_2 + \frac{\beta_3}{(\beta_2 + \beta_3)^2} \theta_2^{(i)} D_1 \right) \right) \right] k^4 \\
& \quad + \left[\frac{\kappa \rho}{\eta} \beta_1^2 (\beta_2 + \beta_3)^2 - (c_0(2\mu + \lambda) + \alpha^2) \beta_1 \frac{\beta_3 - \beta_2 - (\beta_2 + \beta_3)^3}{\beta_2 + \beta_3} \right. \\
& \quad \left. + \gamma \left(-2\beta_1 \beta_3 \theta_2^{(i)} + \beta_1 \beta_3 \theta_1^{(i)} + \beta_1 (\beta_2 + \beta_3)^3 \theta_1^{(i)} - \frac{\beta_1 \beta_3 (\beta_3 - \beta_2)}{(\beta_2 + \beta_3)^3} \theta_2^{(i)} \right) \right] k^2, \\
A_1(k^2) &= \left[\frac{\kappa}{\eta} (2\mu + \lambda) (D_1 + D_2) + (c_0(2\mu + \lambda) + \alpha^2) D_1 D_2 + \frac{\gamma \kappa}{\eta} \left((\beta_2 + \beta_3) \theta_1^{(i)} D_2 + \frac{\beta_3}{(\beta_2 + \beta_3)^2} \theta_2^{(i)} D_1 \right) \right] k^6 \\
& \quad - \left[\frac{\gamma \kappa}{\eta} \left(2\beta_1 \beta_3 \theta_2^{(i)} - \beta_1 \beta_3 \theta_1^{(i)} - \beta_1 (\beta_2 + \beta_3)^3 \theta_1^{(i)} + \frac{\beta_1 \beta_3 (\beta_3 - \beta_2)}{(\beta_2 + \beta_3)^3} \theta_2^{(i)} \right) \right. \\
& \quad \left. + (c_0(2\mu + \lambda) + \alpha^2) \beta_1 \frac{D_2(\beta_3 - \beta_2) - D_1(\beta_2 + \beta_3)^3}{\beta_2 + \beta_3} + \frac{\kappa}{\eta} (2\mu + \lambda) \beta_1 \frac{\beta_3 - \beta_2 - (\beta_2 + \beta_3)^3}{\beta_2 + \beta_3} \right] k^4 \\
& \quad + (c_0(2\mu + \lambda) + \alpha^2) \beta_1^2 (\beta_2 + \beta_3)^2 k^2.
\end{aligned}$$

Due to the high-order of the characteristic polynomial (3.1), it is challenging to determine analytically the main features of the system. We will therefore resort to numerically solving the corresponding eigenvalue systems. Nevertheless, we can observe that for the case that the momentum conservation does not include an acceleration term ($\rho = 0$), the polynomial $P(\phi; k^2)$ is only of order 3. As in [15], we concentrate on distinguishing some particular scenarios that may include or not the inertial term. Unless specified otherwise, throughout our analysis we will employ the following parameter values

$$\begin{aligned}
D_1 &= 0.05, D_2 = 1.0, \beta_1 = 170, \beta_2 = 0.1305, \beta_3 = 0.7695, E = 3 \cdot 10^4, \nu = 0.495, \\
\rho &= 1, c_0 = 1 \cdot 10^{-3}, \kappa = 1 \cdot 10^{-4}, \alpha = 0.1, \eta = 1, \gamma = 1 \cdot 10^{-4},
\end{aligned}$$

which are relevant to the specifications in Tests 1-4 from Section 5. All the computations and graphs in the remainder of this section have been produced with an in-house MATLAB implementation.

3.2. Spatial homogeneous distributions

For the case $k^2 = 0$, the characteristic polynomial $P_2(\phi; 0) = 0$ reduces to

$$P_2(\phi; 0) = \phi^3 \left[\rho c_0 \phi^2 - \rho c_0 \beta_1 \frac{\beta_3 - \beta_2 - (\beta_2 + \beta_3)^3}{\beta_2 + \beta_3} \phi + \rho c_0 \beta_1^2 (\beta_2 + \beta_3)^2 \right].$$

Therefore its roots are either equal to zero or defined by the second-order polynomial in brackets. The so-called Routh-Hurwitz conditions (see e.g. [39]) state that for any polynomial of order 2, a necessary and sufficient set of conditions can be stated so that the roots are in the space of complex non-positive real values, $\mathbb{C} = \{z \in \mathbb{C} : \Re(z) \leq 0\}$. For a general polynomial $P(\phi) = a_2 \phi^2 + a_1 \phi + a_0$, we need to satisfy that all $a_i > 0$ (or all $a_i < 0$). In our case, a_2, a_0 are positive by definition, and consequently the spatial homogeneous case is stable if and only if

$$\beta_3 - \beta_2 < (\beta_2 + \beta_3)^3. \quad (3.2)$$

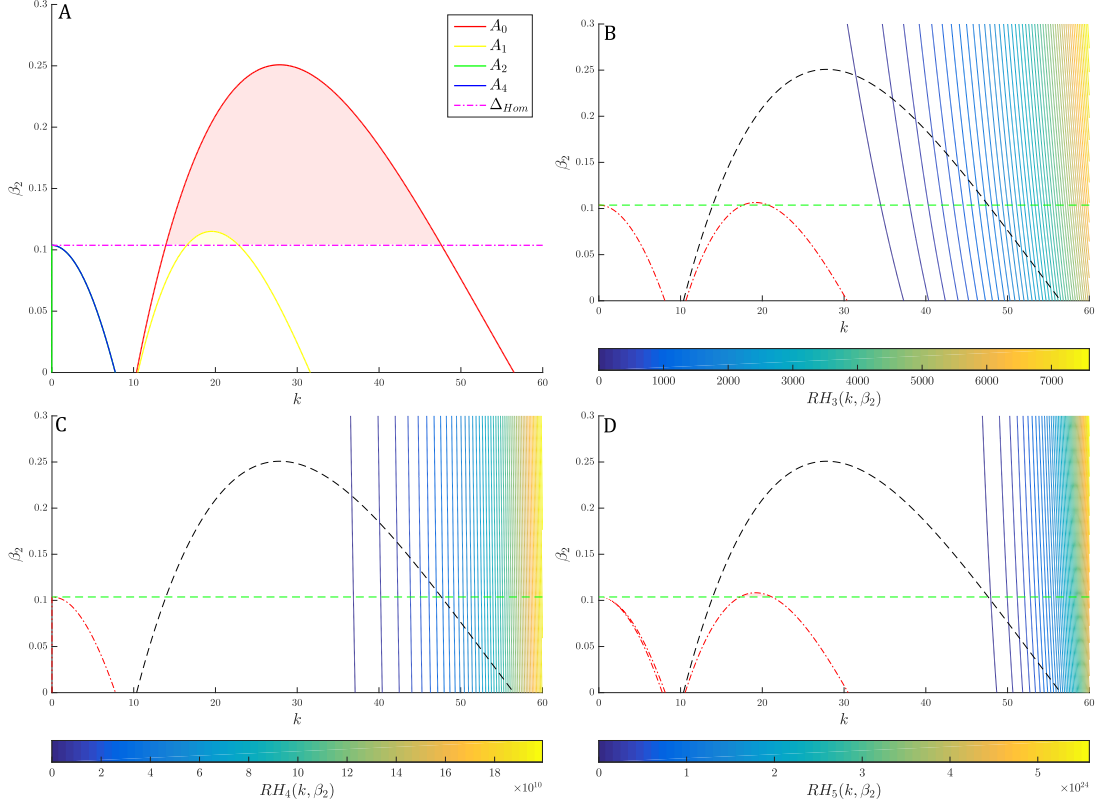


Figure 3.1: Contour plots of the Routh-Hurwitz conditions for the characteristic polynomial of uncoupled system (2.2)-(2.4) with $\rho = 1$. (A) Null level set of P_2 -polynomial coefficients a_i defined in (3.1). a_3 is strictly positive for the selected fixed parameters and so it is not presented. The magenta dot-dashed curve corresponds to the limit of condition (3.2) with fixed $\beta_3 = 0.7695$. (B) Level sets (100) of condition (3.4). Null levels of condition (3.4) (red dot-dashed); a_0 (black dashed); and condition (3.2) (green dashed) are added to locate Turing instability regions. (C-D) Similar analyses for the conditions (3.5) and (3.6) respectively. In all plots, colour-shaded regions correspond to a k - β_2 space that breaks the associated condition.

As β_2, β_3 are positive coefficients, this means that at least the basal source rate β_3 has to be larger than β_2 while their difference is lower than $(\beta_2 + \beta_3)^3$. A similar condition is provided in [24]. Additionally, we observe that the system is homogeneously stable irrespective of the parameter values, by simply imposing that $\rho = 0$, *i.e.*, removing the acceleration term in the momentum equilibrium.

3.3. Uncoupled system

This scenario is reached if either γ or τ (or both) are zero. $P_2(\phi; k^2)$ is then a fifth-order polynomial defined as in 3.1 where the terms including γ or τ are dropped from the coefficients $A_i(k^2)$. For a polynomial of order 5, $P(\phi) = \sum_{j=0}^5 a_j \phi^j$, the Routh-Hurwitz conditions are given by

$$\forall_j \quad a_j > 0, \quad (3.3)$$

$$a_3 a_4 - a_2 a_5 > 0, \quad (3.4)$$

$$a_2 a_3 a_4 - a_2^2 a_5 - a_1 a_4^2 + a_0 a_4 a_5 > 0, \quad (3.5)$$

$$a_0 a_2 a_3 a_4 a_5 - a_0 a_3^2 a_4^2 + a_1 a_2 a_3 a_4^2 - a_1 a_2^2 a_4 a_5 - a_1^2 a_4^3 + 2 a_0 a_1 a_4^2 a_5 - a_0^2 a_4 a_5^2 > 0. \quad (3.6)$$

From (3.2), we see that β_2, β_3 are important parameters of the system. We decide then to perform the analysis with β_2 as variable; fixing all the other parameters. Based on (3.2) and the constrain on the

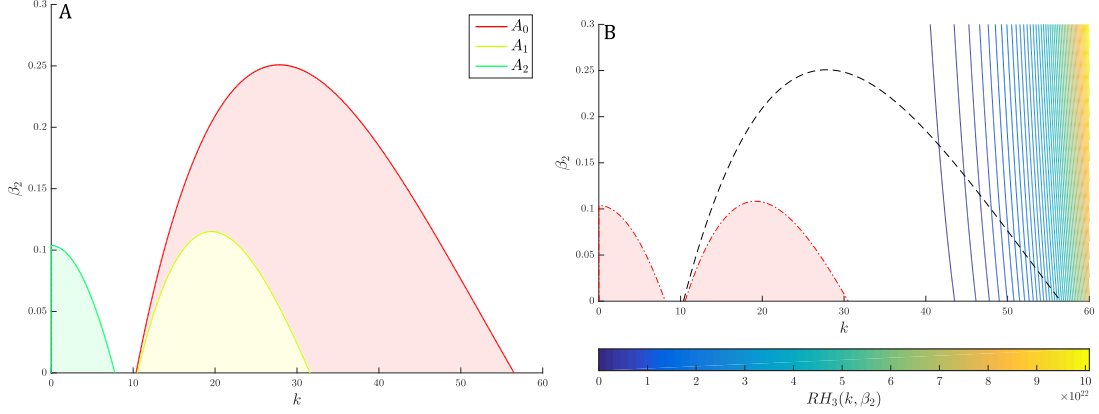


Figure 3.2: Contour plots of the Routh-Hurwitz conditions for the characteristic polynomial of uncoupled system (2.2)-(2.4) with $\rho = 0$. (A) Null level set of P_2 -polynomial coefficients a_i defined in (3.1). a_3 is strictly positive whatever the choice of the parameters and so it is not presented. (B) Level sets (100) of 2nd condition defined in (3.7). Null levels of condition (3.7) (red dot-dashed); and a_0 (black dashed) are added to locate Turing instability regions.

parameters, we deduce easily that conditions a_4 and a_5 are strictly positive, rejecting them to find any patterning space of the system. As the complete analysis of (3.3)-(3.6) is analytically quite involved, we restrict the discussion on the condition that breaks $a_0 > 0$. Beyond its tractable analysis, the choice of this coefficient is legitimised by the fact that a_1, a_2, a_3 can be written as an affine function of a_0 with positive coefficients, as long as $\rho \neq 0$. This leads, in the uncoupled system, to the property that if $a_i > 0$ conditions are broken then $a_0 > 0$ is inevitably unsatisfied.

Figure 3.1(A) plots the contour lines of $a_i, i = 0, \dots, 4$. As we can observe for this specific parameter set, a_2, a_4 are negative only in the region below the magenta dot-dashed curve, corresponding to the limit of the condition (3.2). Consequently, these coefficients are strictly positive while (3.2) is true. Only a_0 and a_1 present Turing instability, and the latter is just a subset of the k - β_2 space defined by a_0 . Conditions (3.4)-(3.6) present a similar behaviour with respect to a_0 (Figs. 3.1(B)-(D)) and so this enables us to focus our linear analysis on the a_0 coefficient only. For the case $\rho = 0$, the resulting polynomial is of order 3 and so the Routh-Hurwitz conditions are defined by

$$\forall_j \quad a_j > 0, \quad a_1 a_2 - a_0 a_3 > 0. \quad (3.7)$$

Note that contrary to the general case, only a_1 can be written as an affine function of a_0 . As the condition (3.2) is no longer needed to obtain homogeneous stability, the coefficients of the affine description of a_1 cannot be said strictly positive as before. Nevertheless, as illustrated in Figure 3.2, condition $a_0 > 0$ is the first to be broken with respect to the value of β_2 , and thus we decide to focus the analysis also on that coefficient.

By definition, a_0 is a polynomial of even order with respect to k^2 , guaranteeing that there exists at least one local extremum. Therefore, we look for the critical wave number $k_c^2 > 0$, obtained by solving the equation $a'_0(k_c^2) = 0$, that substituting in a_0 will lead to the equation $a_0(k_c^2, \varphi_c) = 0$, with φ_c the critical parameter that we want to analyse. In the studied scenario, a'_0 is a cubic polynomial with respect to k^2 , and from the Routh-Hurwitz conditions, the following criteria might be satisfied in order for a_0 to be negative for a positive k^2

$$D_2(\beta_3 - \beta_2) - D_1(\beta_2 + \beta_3)^3 > 0, \quad (3.8)$$

$$36 \left(\beta_1 \frac{D_2(\beta_3 - \beta_2) - D_1(\beta_2 + \beta_3)^3}{\beta_2 + \beta_3} \right)^2 (\beta_1^2(\beta_2 + \beta_3)^2)^2 - 128 D_1 D_2 (\beta_1^2(\beta_2 + \beta_3)^2)^3 > 0. \quad (3.9)$$

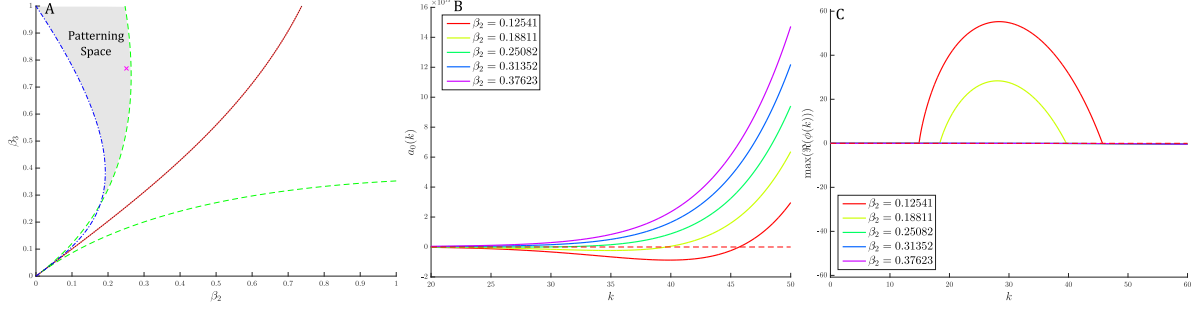


Figure 3.3: Patterning space, parameter condition and dispersion relations for the uncoupled poromechano-chemical model. (A) Predicted patterning space for a selected interval in (β_2, β_3) parameter space: boundary constructed from (3.8) (red plain); from (3.9) (green-dashed); and from (3.2) (blue-dot-dashed). (B) Parameter coefficient condition a_0 . Curves are drawn from the critical value $\beta_{2,c}$ (green) and for 25% and 50% increase/decrease of the parameter values. The critical parameter value is located in (A) and denoted by a magenta cross. (C) Associated dispersion relations, where the colour code is kept identical as in (B).

Inequality (3.8) enforces that the coefficient has a real positive part and it comes from the analysis of the Routh-Hurwitz conditions. Combined with condition (3.2), it gives an interval for the ratio $(\beta_2 + \beta_3)^3/(\beta_3 - \beta_2)$ parameter where Turing instabilities are reached. As the discriminant of a_0 is null, we look for the discriminant (3.9) of the derivative a'_0 to force $k^2 \in \mathbb{R}$. Figure 3.3 (panels (A)-(C)) present the patterning space based on the implicit functions defined in (3.8) and (3.9) for the (β_2, β_3) space. Figure 3.3 suggests that increasing the value of the production basal rate (β_3) of the inhibitor w_2 leads to an interval augmentation of possible basal rate (β_2) of the activator w_1 . The condition (3.2) represented by the blue-dot-dashed curve in Figure 3.3(A) is absent for the $\rho = 0$ scenario, leading to an increase of the patterning space region. Thus, introducing acceleration in the momentum equilibrium equation leads to a restriction of the Turing space.

3.4. Coupled system - Null production/degradation rates

In contrast with other reaction-diffusion systems, due to the coupling with the poroelastic deformations we can perfectly have situations where production/degradation rates are missing. For the first case of $\beta_1 = 0$, corresponding to a pure advection-diffusion chemical system, the characteristic polynomial for $\rho \neq 0$ is still of order 5 with the new coefficients

$$\begin{aligned}
 A_5^{(1)}(k^2) &= A_5(k^2), & A_4^{(1)}(k^2) &= \rho \left(c_0(D_1 + D_2) + \frac{\kappa}{\eta} \right) k^2, \\
 A_3^{(1)}(k^2) &= \rho \left(\frac{\kappa}{\eta}(D_1 + D_2) + c_0 D_1 D_2 \right) k^4 + \left[c_0(2\mu + \lambda) + \alpha^2 + \gamma c_0 \left((\beta_2 + \beta_3)\theta_1^{(i)} + \frac{\beta_3}{(\beta_2 + \beta_3)^2}\theta_2^{(i)} \right) \right] k^2, \\
 A_2^{(1)}(k^2) &= \frac{\kappa\rho}{\eta} D_1 D_2 k^6 + \left[(c_0(2\mu + \lambda) + \alpha^2)(D_1 + D_2) + \frac{\kappa}{\eta}(2\mu + \lambda) \right. \\
 &\quad \left. + \gamma \left(\frac{\kappa}{\eta} \left((\beta_2 + \beta_3)\theta_1^{(i)} + \frac{\beta_3}{(\beta_2 + \beta_3)^2}\theta_2^{(i)} \right) + c_0 \left((\beta_2 + \beta_3)\theta_1^{(i)} D_2 + \frac{\beta_3}{(\beta_2 + \beta_3)^2}\theta_2^{(i)} D_1 \right) \right) \right] k^4, \\
 A_1^{(1)}(k^2) &= \left[\frac{\kappa}{\eta}(2\mu + \lambda)(D_1 + D_2) + (c_0(2\mu + \lambda) + \alpha^2) D_1 D_2 + \frac{\gamma\kappa}{\eta} \left((\beta_2 + \beta_3)\theta_1^{(i)} D_2 + \frac{\beta_3}{(\beta_2 + \beta_3)^2}\theta_2^{(i)} D_1 \right) \right] k^6, \\
 A_0^{(1)}(k^2) &= \frac{\kappa}{\eta}(2\mu + \lambda) D_1 D_2 k^8,
 \end{aligned}$$

where each $\theta^{(i)}$ (for $i = 1, 2$) is specified as

$$\theta^{(1)} = \begin{pmatrix} \theta_1^{(1)} \\ \theta_2^{(1)} \end{pmatrix} = -\tau(1, 1)^T, \quad \theta^{(2)} = -2\tau(1, 0)^T. \quad (3.10)$$

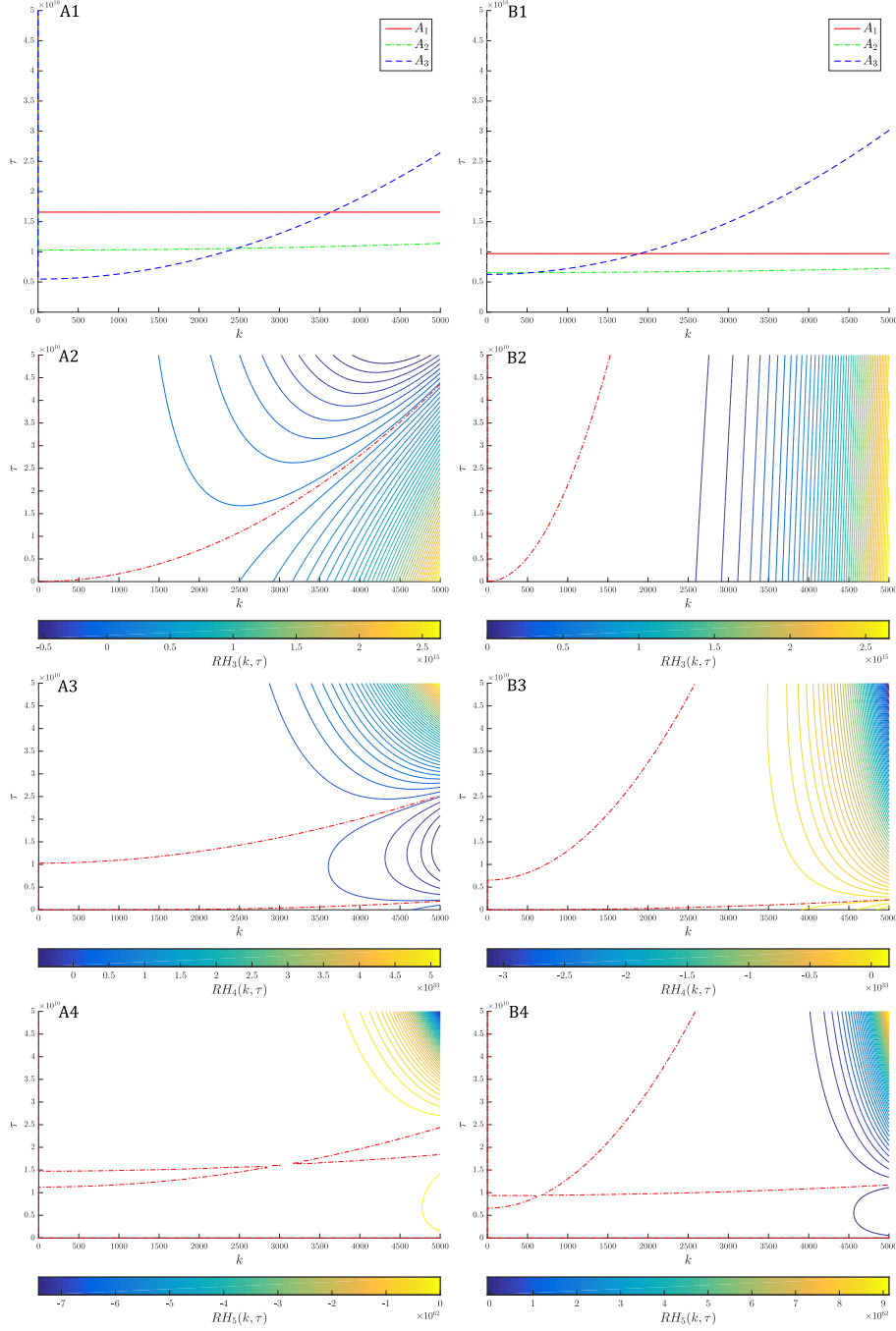


Figure 3.4: Contour plots of the Routh-Hurwitz conditions for the characteristic polynomial of system (2.2)-(2.4) for $\beta_1 = 0$ and $\rho = 1$. (A1) Null level set of P_2 -polynomial coefficients $a_i^{(1)}$ for the coupling term $\theta^{(1)}$. (A2) Level sets (100) of condition (3.4) with null level of the condition (3.4) (red dot-dashed) for the coupling term $\theta^{(1)}$. (A3-A4) Similar analysis for the conditions (3.5) and (3.6) respectively. (B1-B4) Similar analysis for the coupling term $\theta^{(2)}$.

By definition, we observe that the spatial homogeneous situation ($k = 0$) is stable whatever the value of the parameters. For a general k , all the coefficients that do not include the coupling parameter γ are

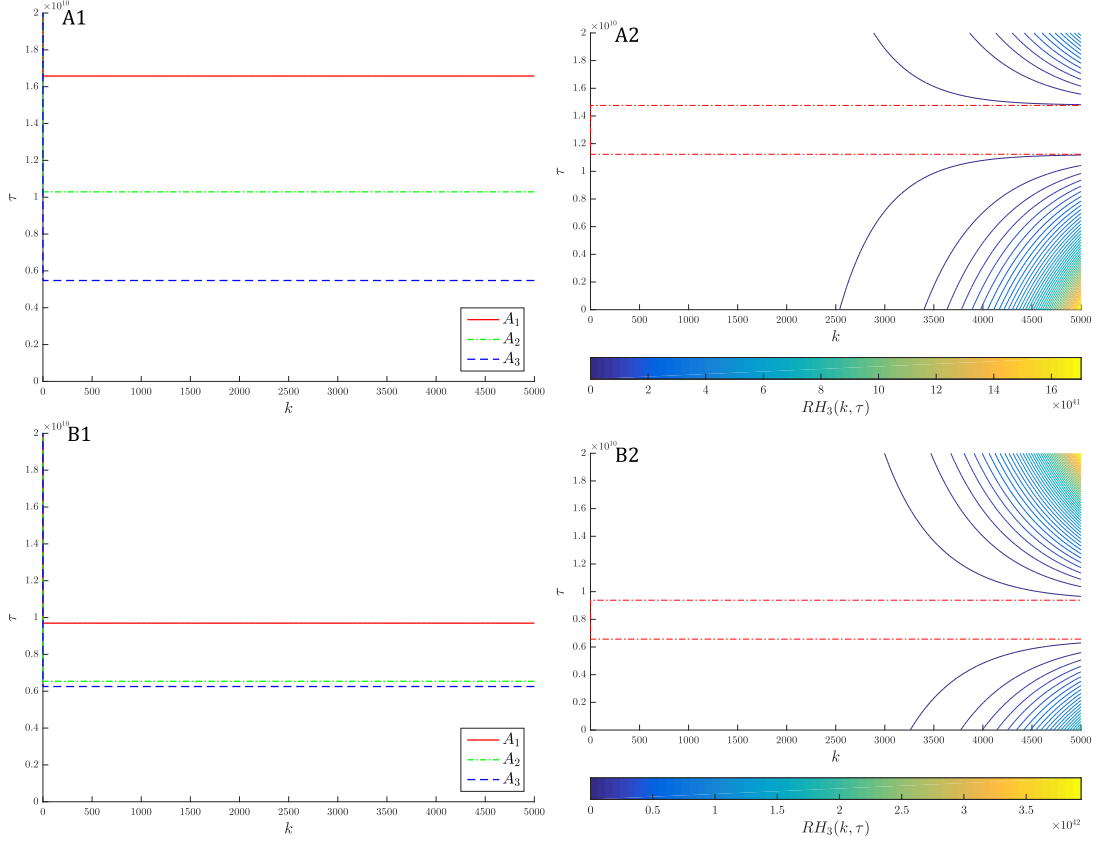


Figure 3.5: Contour plots of the Routh-Hurwitz conditions for the characteristic polynomial of system (2.2)-(2.4) for $\beta_1 = 0$ and $\rho = 0$. (A1) Null level set of P_2 -polynomial coefficients $a_i^{(1)}$ for the coupling term $\theta^{(1)}$. (A2) Level sets (100) of condition (3.7) with associated null level (red dot-dashed) for the coupling term $\theta^{(1)}$. (B1-B2) Similar analysis for the coupling term $\theta^{(2)}$.

strictly positive, and consequently they do not influence the stability of the coupled system. As there is no restriction on the choice of the parameter values for the homogeneous case, any parameter can be chosen as the critical one. In order to analyse the influence of poromechanics on the chemical system, we regard τ as the parameter of interest.

Figure 3.4 presents contour plots of the Routh-Hurwitz conditions with respect to wave number k and parameter τ for both θ defined in (3.10). From Figures 3.4(A1) and 3.4(B1), we observe that a_3 is the first coefficient to break the inequality condition with respect to τ , at a low wave number. Along k , the parabolic shape of the null levels shows how, depending on the size of the system, any of the three coefficients can break the Routh-Hurwitz inequality. Consequently, the coupled system presents complex instability behaviour and makes difficult to choose only one of them to analyse the full patterning space. Nevertheless, patterns are reachable for large values of τ , irrespective of the wave number (at least in the presented interval). This is contrary to the uncoupled case, where all the a_i 's are strictly positive. Figures 3.4(A2)-(A4) and 3.4(B2)-(B4) display the sign of the conditions (3.4)-(3.6) for $\theta^{(1)}$ and $\theta^{(2)}$, respectively. We readily see that the instability region starts already at a value of τ ($\sim 10^5$) lower than that provided by the a_i 's. This emphasises the influence of the mechanical coupling into pattern formation.

The choice of the coupling function θ has a non-intuitive influence on the Routh-Hurwitz condi-

tions. While it reduces the area of instability region for conditions (3.4) and (3.6) (cf. respectively Figs. 3.4(A2), (B2) and Figs. 3.4(A4), (B4)), it increases it for condition (3.5) (cf. Figs. 3.4(A3), (B3)). Proposing a patterning space based uniquely on the parameters can still be quite difficult due to the complexity of the Routh-Hurwitz conditions and by the evolution of the inequality constrain through the wave number. Nonetheless, we can still show how the poromechanics coupled to a pure advection-diffusion system might generate patterns. In the absence of acceleration, the analysis of the Routh-Hurwitz conditions is quite similar (see Figure 3.5) to the general case. We observe again that for a specific τ , the conditions can break for any coupling function θ . Contrary to the case of $\rho = 1$, here the defect on the criteria occurs almost at one specific value of τ for any wave number k (see Figs. 3.5(A1), (B1)). The coupling function seems to move closer to each other the levels of the different coefficients a_i , and it also decreases the interval of τ that leads to breaking the second condition (3.7).

Secondly, we impose either the basal rate of the activator, β_2 , or the inhibitor, β_3 , to be equal to zero. Again the characteristic polynomial $P_2(\phi, k^2)$ for $\rho \neq 0$ is still of order 5 with the new coefficients given by

$$\begin{aligned}
A_5^{(2)}(k^2) &= A_5^{(3)}(k^2) = A_5(k^2), \quad A_4^{(2,3)}(k^2) = \rho \left(c_0(D_1 + D_2) + \frac{\kappa}{\eta} \right) k^2 - \begin{cases} \rho c_0 \beta_1 (1 - \beta_3^2) \\ -\rho c_0 \beta_1 (1 + \beta_2^2) \end{cases} \\
A_3^{(2,3)}(k^2) &= \rho \left(\frac{\kappa}{\eta} (D_1 + D_2) + c_0 D_1 D_2 \right) k^4 \\
&\quad + \begin{cases} \left[c_0(2\mu + \lambda) + \alpha^2 - \rho c_0 \beta_1 (D_2 - D_1 \beta_3^2) - \frac{\kappa \rho}{\eta} \beta_1 (1 - \beta_3^2) + \Psi(\beta_3; \tau) \right] k^2 + c_0 \rho \beta_1^2 \beta_3^2 \\ \left[c_0(2\mu + \lambda) + \alpha^2 + \rho c_0 \beta_1 (D_2 + D_1 \beta_2^2) + \frac{\kappa \rho}{\eta} \beta_1 (1 + \beta_2^2) + \Psi(\beta_2; \tau) \right] k^2 + c_0 \rho \beta_1^2 \beta_2^2 \end{cases} \\
A_2^{(2,3)} &= \frac{\kappa \rho}{\eta} D_1 D_2 k^6 \\
&\quad + \begin{cases} \left[(c_0(2\mu + \lambda) + \alpha^2) (D_1 + D_2) + \frac{\kappa}{\eta} (2\mu + \lambda) - \frac{\kappa \rho}{\eta} \beta_1 (D_2 - D_1 \beta_3^2) + \Psi(\beta_3; \tau) \right] k^4 \\ \left[(c_0(2\mu + \lambda) + \alpha^2) (D_1 + D_2) + \frac{\kappa}{\eta} (2\mu + \lambda) + \frac{\kappa \rho}{\eta} \beta_1 (D_2 + D_1 \beta_2^2) + \Psi(\beta_2; \tau) \right] k^4 \end{cases} \\
&\quad + \begin{cases} \left[\frac{\kappa \rho}{\eta} \beta_1^2 \beta_3^2 - (c_0(2\mu + \lambda) + \alpha^2) \beta_1 (1 - \beta_3^2) + \Psi(\beta_3; \tau) \right] k^2 \\ \left[\frac{\kappa \rho}{\eta} \beta_1^2 \beta_2^2 + (c_0(2\mu + \lambda) + \alpha^2) \beta_1 (1 + \beta_2^2) + \Psi(\beta_2; \tau) \right] k^2 \end{cases} \\
A_1^{(2,3)} &= \begin{cases} \left[\frac{\kappa}{\eta} (2\mu + \lambda) (D_1 + D_2) + (c_0(2\mu + \lambda) + \alpha^2) D_1 D_2 + \Psi(\beta_3; \tau) \right] k^6 \\ \left[\frac{\kappa}{\eta} (2\mu + \lambda) (D_1 + D_2) + (c_0(2\mu + \lambda) + \alpha^2) D_1 D_2 + \Psi(\beta_2; \tau) \right] k^6 \end{cases} \\
&\quad - \begin{cases} \left[(c_0(2\mu + \lambda) + \alpha^2) \beta_1 (D_2 - D_1 \beta_3^2) + \frac{\kappa}{\eta} (2\mu + \lambda) \beta_1 (1 - \beta_3^2) + \Psi(\beta_3; \tau) \right] k^4 \\ - \left[(c_0(2\mu + \lambda) + \alpha^2) \beta_1 (D_2 + D_1 \beta_2^2) + \frac{\kappa}{\eta} (2\mu + \lambda) \beta_1 (1 + \beta_2^2) - \Psi(\beta_2; \tau) \right] k^4 \end{cases} \\
&\quad + \begin{cases} (c_0(2\mu + \lambda) + \alpha^2) \beta_1^2 \beta_3^2 k^2 \\ (c_0(2\mu + \lambda) + \alpha^2) \beta_1^2 \beta_2^2 k^2 \end{cases} \\
A_0^{(2,3)} &= \begin{cases} \frac{\kappa}{\eta} (2\mu + \lambda) k^4 [D_1 D_2 k^4 - \beta_1 (D_2 - D_1 \beta_3^2) k^2 + \beta_1^2 \beta_3^2] \\ \frac{\kappa}{\eta} (2\mu + \lambda) k^4 [D_1 D_2 k^4 + \beta_1 (D_2 + D_1 \beta_2^2) k^2 + \beta_1^2 \beta_2^2] \end{cases}
\end{aligned}$$

where Ψ is a generic function that summarises the appropriate coupling term defined precisely in (3.1) and the upper (resp. lower) line in braces exhibits the coefficient description for $\beta_2 = 0$ (resp. $\beta_3 = 0$). We observe from the new set of coefficients that the stability of the system behaves differently with respect to the basal rate imposed to zero. In an uncoupled scenario, the case $\beta_3 = 0$ presents a_i 's coefficients that are strictly positive whatever the value of the coefficients. This indicates that removing the basal production of the inhibitor prevents any patterning (in the uncoupled scenario), and this occurs for any ρ and any wave number k . For $\beta_2 = 0$, the system can enter an instability region if and

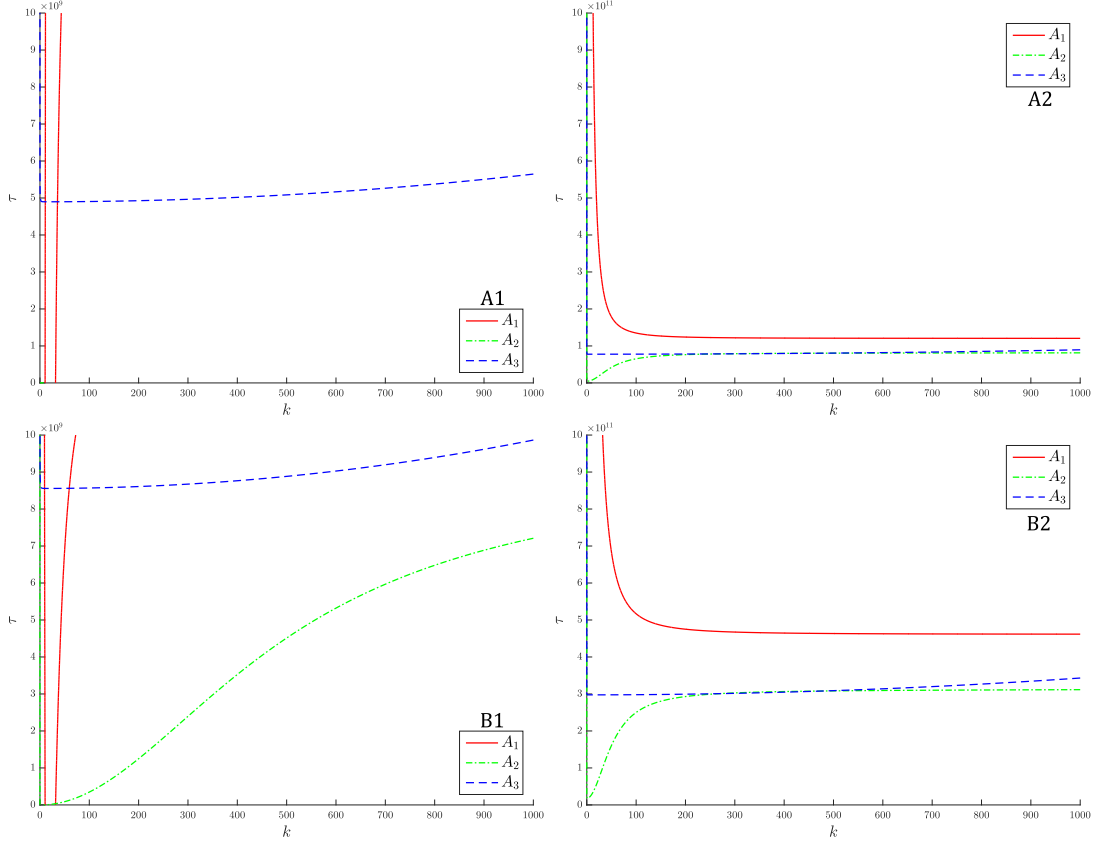


Figure 3.6: Null level set of the characteristic polynomial coefficients $a_i^{(2,3)}$ defined in (3.1) for different null basal rate and coupling term θ . (A1) $\beta_2 = 0$ with $\theta^{(1)}$. (A2) $\beta_3 = 0$ with $\theta^{(1)}$. (B1-B2) Similar analysis for $\theta^{(2)}$. In all plots, the density of the solid material is $\rho = 1$.

only if

$$0 < \beta_3 < \sqrt{\min\left(1, \frac{D_2}{D_1}\right)}.$$

Coupling the advection-reaction-diffusion system to the poromechanics enables both scenarios to reach instability depending on the parameter values. We analyse again our system focusing on τ . Figure 3.6 presents the null level set of the coefficients for both θ (cf. (3.10)) and for $\rho = 1$. The case $\beta_2 = 0$ (see Figs. 3.6(A1), (B1)) is significantly influenced by the choice of θ . Going from a linear $\theta^{(1)}$ to a nonlinear $\theta^{(2)}$ coupling function, the instability region is clearly modified, especially for the coefficient a_2 , leading to an increase of its area. Furthermore, starting from some wave number k , the system presents instability whatever the choice of the parameter τ (e.g., red null level in Fig. 3.6(A1)). In $\beta_3 = 0$, instabilities can be produced using a large value of τ (see Figs. 3.6(A2), (B2)), implying that coupling the advection-reaction-diffusion system to a mechanical one enables us to bypass the intrinsic stability of the system determined by $\beta_3 = 0$ in an uncoupled scenario, as pointed out above.

3.5. General System

In a general scenario, we look how the strength of the coupling between the poromechanical and chemical system can affect its linear stability. Figures 3.7 present, for different values of γ (which we

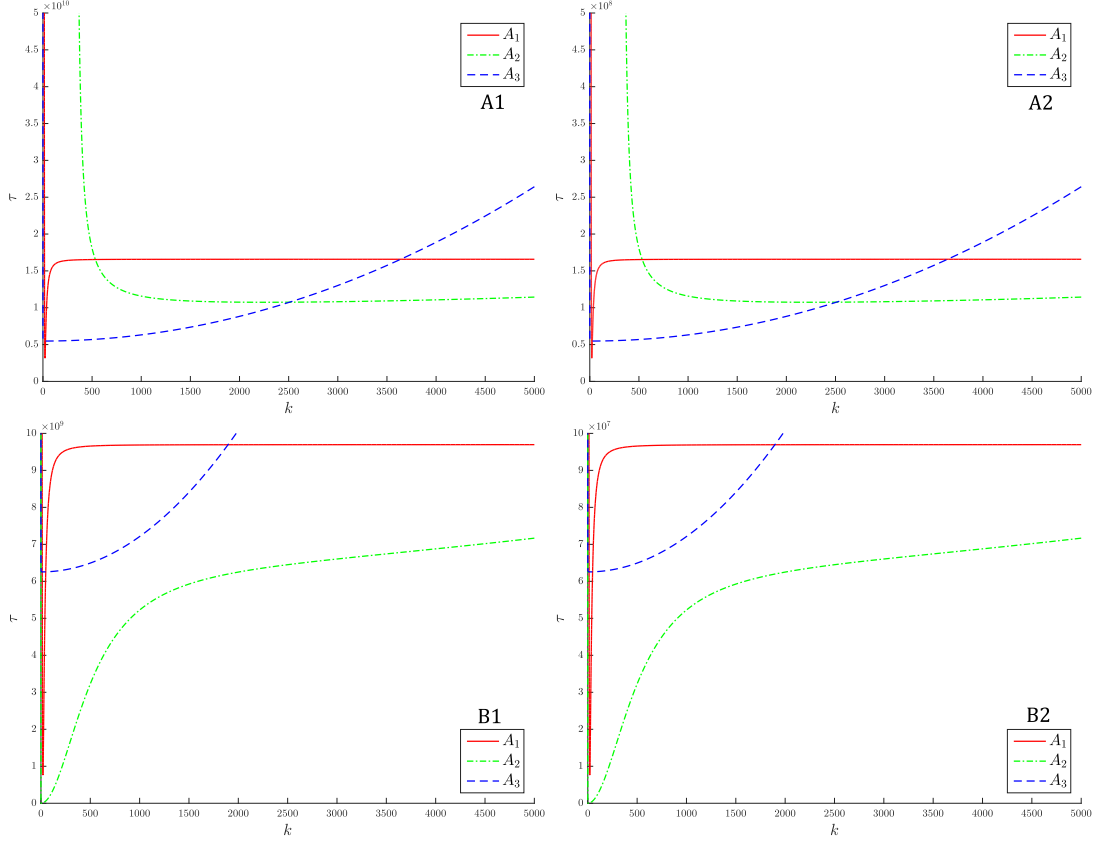


Figure 3.7: Null level set of the characteristic polynomial coefficients a_i with respect to τ defined in (3.1) for the general coupled system and for different coupling term θ . (A1) $\gamma = 10^{-4}$ with $\theta^{(1)}$. (A2) $\gamma = 10^{-2}$ with $\theta^{(1)}$. (B1-B2) Similar analysis for $\theta^{(2)}$. In all plots, the density of the solid material is imposed to $\rho = 1$.

recall is parameter that couples the poroelasticity to the Schnakenberg model), the null levels of the dispersion relation coefficients. Increasing γ leads to a reduction of the critical value of τ needed to reach instability (compare with Figs. 3.7(A1), (A2)) without affecting the pattern generated by the null level set. Analogous conclusions can be drawn even using a nonlinear coupling function $r^{(2)}(w)$. As in the previous scenario, the different coefficients present a large interval where the Routh-Hurwitz conditions are not satisfied. In summary, the coupled system accommodates the possibility of generating patterns at different length scales.

To conclude this section, we analyse the sign of the a_i coefficients against the value of β_2 , and compare with the results from the uncoupled model studied above. Figures 3.8 display the null level set for an increasing strength of the coupling by augmenting both the value of τ and γ . From Figure 3.8(A1) to 3.8(A3), we observe that a_2 is particularly affected by the choice of these two parameters. First reducing the region of instability (see Fig. 3.8(A2)), we obtain, in a more strongly coupled system, two instability regions delimited by the red (a_0) and green (a_2) level sets that overlap with respect to the wave number k , but not with respect to β_2 . Consequently, and depending on the strength of the coupling between reaction-diffusion and poroelastic effects, we can discriminate different values of β_2 that will produce distinct patterns at desired specific scales. This is more clearly seen for the case with $\theta = \theta^{(2)}$, where the interval of β_2 that leads to instability increases rapidly with the augmentation of τ and γ , and tends finally to overlap the region delimited by a_0 (see red level in Fig. 3.8(B3)).

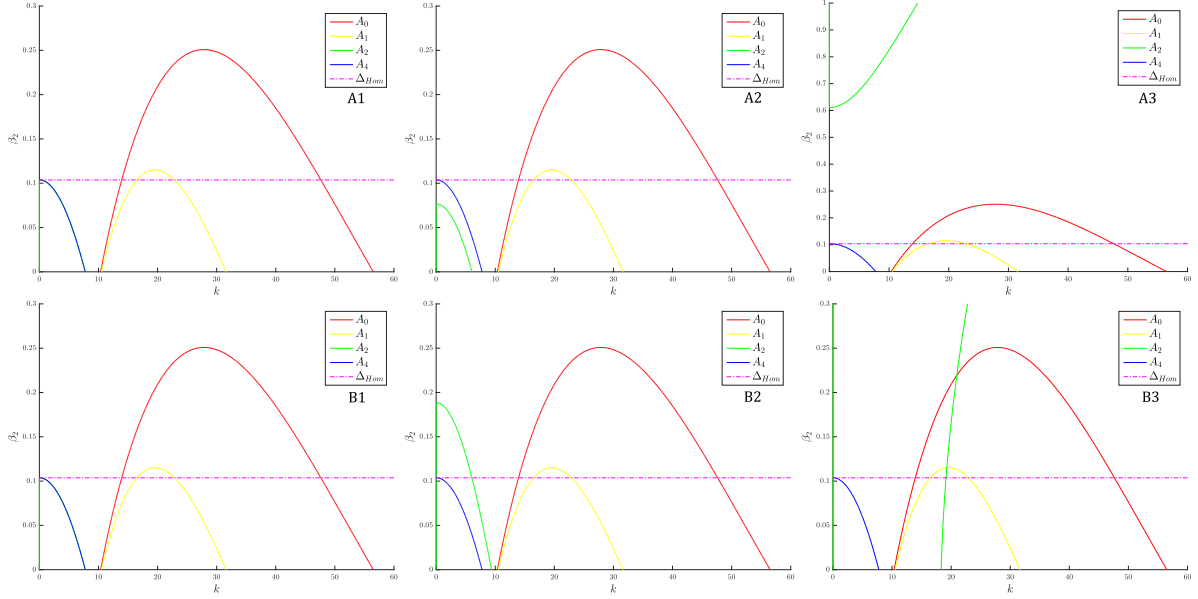


Figure 3.8: Null level set of the characteristic polynomial coefficients a_i with respect to β_2 defined in (3.1) for the general coupled system and for different coupling term θ . (A1) $\tau = 100$, $\gamma = 10^{-4}$, with $\theta^{(1)}$. (A2) $\tau = 10^4$, $\gamma = 10^{-2}$ with $\theta^{(1)}$. (A3) $\tau = 10^5$, $\gamma = 10^{-2}$ with $\theta^{(1)}$. (B1-B3) Similar analysis with $\theta^{(2)}$. In all plots, the density of the solid material is imposed to $\rho = 1$.

4. Numerical method and implementation

In [49] we propose a discretisation in space using a mixed finite element method. In the lowest-order case, the method consists of piecewise bilinear elements enriched with bubbles for the displacement, piecewise linear and continuous approximations for the fluid pressure and for the solutes, and piecewise constant approximation for total pressure.

The time discretisation is achieved by a backward Euler scheme and an implicit centred difference method for the first and second order time derivatives, respectively. Denoting

$$\delta_t X^{n+1} := \frac{X^{n+1} - X^n}{\Delta t}, \quad \delta_{tt} X^{n+1} := \frac{X^{n+1} - 2X^n + X^{n-1}}{\Delta t^2},$$

the fully discrete method reads: From initial data $\mathbf{u}^{s,0}, p^{f,0}, \psi^0, w_1^0, w_2^0$ (which will be projections of the continuous initial conditions of each field) and for $n = 1, \dots$, find $\mathbf{u}_h^{s,n+1} \in \mathbf{V}_h, p_h^{f,n+1} \in Q_h, \psi_h^{n+1} \in Z_h, w_{1,h}^{n+1} \in W_h, w_{2,h}^{n+1} \in W_h$ such that

$$\tilde{a}_1(\mathbf{u}_h^{s,n+1}, \mathbf{v}_h^s) + a_1(\mathbf{u}_h^{s,n+1}, \mathbf{v}_h^s) + b_1(\mathbf{v}_h^s, \psi_h^{n+1}) = F_{r_h^{n+1}}(\mathbf{v}_h^s) \quad \forall \mathbf{v}_h^s \in \mathbf{V}_h, \quad (4.1)$$

$$\tilde{a}_2(p_h^{f,n+1}, q_h^f) + a_2(p_h^{f,n+1}, q_h^f) - b_2(q_h^f, \delta_t \psi_h^{n+1}) = G_{\ell^{n+1}}(q_h^f) \quad \forall q_h^f \in Q_h, \quad (4.2)$$

$$b_1(\mathbf{u}_h^{s,n+1}, \phi_h) + b_2(p_h^{f,n+1}, \phi_h) - a_3(\psi_h^{n+1}, \phi_h) = 0 \quad \forall \phi_h \in Z_h, \quad (4.3)$$

$$\tilde{a}_4(w_{1,h}^{n+1}, s_{1,h}) + a_4(w_{1,h}^{n+1}, s_{1,h}) = J_{f_h^{n+1}}(s_{1,h}) \quad \forall s_{1,h} \in W_h, \quad (4.4)$$

$$\tilde{a}_5(w_{2,h}^{n+1}, s_{2,h}) + a_5(w_{2,h}^{n+1}, s_{2,h}) = J_{g_h^{n+1}}(s_{2,h}) \quad \forall s_{2,h} \in W_h. \quad (4.5)$$

with

$$\tilde{a}_1(\mathbf{u}_h^{s,n+1}, \mathbf{v}_h^s) := \int_{\Omega} \delta_{tt} \mathbf{u}_h^{s,n+1} \cdot \mathbf{v}_h, \quad a_1(\mathbf{u}_h^{s,n+1}, \mathbf{v}_h^s) := 2\mu \int_{\Omega} \varepsilon(\mathbf{u}_h^{s,n+1}) : \varepsilon(\mathbf{v}_h^s),$$

$$\begin{aligned}
b_1(\mathbf{v}_h^s, \phi_h) &:= - \int_{\Omega} \phi_h \operatorname{div} \mathbf{v}_h^s, \quad b_2(p_h^{f,n+1}, \phi_h) := \frac{\alpha}{\lambda} \int_{\Omega} p_h^{f,n+1} \phi_h, \quad a_3(\psi_h^{n+1}, \phi_h) := \frac{1}{\lambda} \int_{\Omega} \psi_h^{n+1} \phi_h, \\
\tilde{a}_2(p_h^{f,n+1}, q_h^f) &:= \left(c_0 + \frac{\alpha^2}{\lambda} \right) \int_{\Omega} \delta_t p_h^{f,n+1} q_h^f, \quad a_2(p_h^{f,n+1}, q_h^f) := \frac{1}{\eta} \int_{\Omega} \kappa \nabla p_h^{f,n+1} \cdot \nabla q_h^f, \\
\tilde{a}_4(w_{1,h}^{n+1}, s_{1,h}) &:= \delta_t \int_{\Omega} w_{1,h}^{n+1} s_{1,h}, \quad a_4(w_{1,h}^{n+1}, s_{1,h}) := \int_{\Omega} D_1(\mathbf{x}) \nabla w_{1,h}^{n+1} \cdot \nabla s_{1,h}, \\
\tilde{a}_5(w_{2,h}^{n+1}, s_{2,h}) &:= \delta_t \int_{\Omega} w_{2,h}^{n+1} s_{2,h}, \quad a_5(w_{2,h}^{n+1}, s_{2,h}) := \int_{\Omega} D_2(\mathbf{x}) \nabla w_{2,h}^{n+1} \cdot \nabla s_{2,h}, \\
F_{r_h^{n+1}}(\mathbf{v}_h^s) &:= \rho \int_{\Omega} \mathbf{b}^{n+1} \cdot \mathbf{v}_h^s + \tau \int_{\Omega} r_h^{n+1} \mathbf{k} \otimes \mathbf{k} : \boldsymbol{\varepsilon}(\mathbf{v}_h^s), \\
G_{\ell^{n+1}}(q_h^f) &:= \int_{\Omega} \ell^{n+1} q_h^f, \quad J_{f^{n+1}}(s_{1,h}) := \int_{\Omega} f^{n+1} s_{1,h}, \quad J_{g^{n+1}}(s_{2,h}) := \int_{\Omega} g^{n+1} s_{2,h}.
\end{aligned} \tag{4.6}$$

and where for the treatment of the ADR problem, we have proceeded as in [29]. The only nonlinearities reside in the terms $F_{r_h^{n+1}}(\mathbf{v}_h^s)$, $J_{f^{n+1}}(s_{1,h})$, and $J_{g^{n+1}}(s_{2,h})$.

With the aim to rewrite the Galerkin scheme (4.1)-(4.5) as a matrix equation, we begin by decomposing the unknowns $\mathbf{u}_h^s, \psi_h, p_h, w_{1,h}$ and $w_{2,h}$ in terms of the linear basis functions:

$$\mathbf{u}_h^s = \sum_{j=1}^{N_1} U_j \boldsymbol{\varphi}_j, \quad \psi_h = \sum_{j=1}^{N_2} \Phi_j \hat{\varphi}_j, \quad p_h = \sum_{j=1}^{N_3} P_j \tilde{\varphi}_j, \quad w_{1,h} = \sum_{j=1}^{N_4} W_{1,j} \bar{\varphi}_j, \quad w_{2,h} = \sum_{j=1}^{N_4} W_{2,j} \bar{\varphi}_j,$$

and substituting in the above equations

$$\begin{aligned}
&\sum_{j=1}^{N_1} (\boldsymbol{\varphi}_j, \boldsymbol{\varphi}_i) U_j^{n+1} + \Delta t^2 \sum_{j=1}^{N_1} a_1(\boldsymbol{\varphi}_j, \boldsymbol{\varphi}_i) U_j^{n+1} + \Delta t^2 \sum_{j=1}^{N_2} b_1(\boldsymbol{\varphi}_i, \hat{\varphi}_j) \Phi_j^{n+1} = \Delta t^2 \sum_{j=1}^{N_1} F_{r_h^{n+1}}(\boldsymbol{\varphi}_i) \\
&\quad + \sum_{j=1}^{N_1} (\boldsymbol{\varphi}_j, \boldsymbol{\varphi}_i) U_j^n - \sum_{j=1}^{N_1} (\boldsymbol{\varphi}_j, \boldsymbol{\varphi}_i) U_j^{n-1} \quad i = 1, \dots, N_1, \\
&\left(c_0 + \frac{\alpha^2}{\lambda} \right) \sum_{j=1}^{N_3} (\tilde{\varphi}_j, \tilde{\varphi}_i) P_j^{n+1} + \Delta t \sum_{j=1}^{N_3} a_2(\tilde{\varphi}_j, \tilde{\varphi}_i) P_j^{n+1} - \sum_{j=1}^{N_2} b_2(\tilde{\varphi}_i, \hat{\varphi}_j) \Phi_j^{n+1} = \Delta t \sum_{j=1}^{N_3} G(\tilde{\varphi}_i) \\
&\quad + \left(c_0 + \frac{\alpha^2}{\lambda} \right) \sum_{j=1}^{N_3} (\tilde{\varphi}_j, \tilde{\varphi}_i) P_j^n - \sum_{j=1}^{N_2} b_2(\tilde{\varphi}_i, \hat{\varphi}_j) \Phi_j^n \quad i = 1, \dots, N_3, \\
&\sum_{j=1}^{N_1} b_1(\boldsymbol{\varphi}_j, \hat{\varphi}_i) U_j^{n+1} + \sum_{j=1}^{N_3} b_2(\tilde{\varphi}_j, \hat{\varphi}_i) P_j^{n+1} - \sum_{j=1}^{N_2} a_3(\hat{\varphi}_j, \hat{\varphi}_i) \Phi_j^{n+1} = 0 \quad i = 1, \dots, N_2, \\
&\sum_{j=1}^{N_4} (\bar{\varphi}_j, \bar{\varphi}_i) W_j^{n+1} - \Delta t \sum_{j=1}^{N_4} a_4(\bar{\varphi}_j, \bar{\varphi}_i) W_j^{n+1} = \Delta t \sum_{j=1}^{N_4} J_{f^{n+1}}(\bar{\varphi}_i) + \sum_{j=1}^{N_4} (\bar{\varphi}_j, \bar{\varphi}_i) W_j^n \quad i = 1, \dots, N_4, \\
&\sum_{j=1}^{N_4} (\bar{\varphi}_j, \bar{\varphi}_i) W_j^{n+1} - \Delta t \sum_{j=1}^{N_4} a_5(\bar{\varphi}_j, \bar{\varphi}_i) W_j^{n+1} = \Delta t \sum_{j=1}^{N_4} J_{g^{n+1}}(\bar{\varphi}_i) + \sum_{j=1}^{N_4} (\bar{\varphi}_j, \bar{\varphi}_i) W_j^n \quad i = 1, \dots, N_4.
\end{aligned}$$

Then, we can organise the above system in terms of matrices and vectors:

$$\begin{aligned}
\tilde{A}_1 &\in \mathbf{R}^{N_1 \times N_1}, \quad A_1 \in \mathbf{R}^{N_1 \times N_1}, \quad B_1 \in \mathbf{R}^{N_2 \times N_1}, \quad B_2 \in \mathbf{R}^{N_3 \times N_2}, \quad \tilde{A}_2 \in \mathbf{R}^{N_3 \times N_3}, \quad A_2 \in \mathbf{R}^{N_3 \times N_3}, \\
A_3 &\in \mathbf{R}^{N_2 \times N_2}, \quad \tilde{A}_4 \in \mathbf{R}^{N_4 \times N_4}, \quad A_4 \in \mathbf{R}^{N_4 \times N_4}, \quad \tilde{A}_5 \in \mathbf{R}^{N_4 \times N_4}, \quad A_5 \in \mathbf{R}^{N_4 \times N_4}, \\
F &\in \mathbf{R}^{N_1}, \quad G \in \mathbf{R}^{N_3}, \quad J_1 \in \mathbf{R}^{N_4}, \quad J_2 \in \mathbf{R}^{N_4},
\end{aligned}$$

such that

$$\begin{aligned}
\tilde{a}_{1,ij} &= (\varphi_j, \varphi_i), & a_{1,ij} &= \Delta t^2 a_1(\varphi_j, \varphi_i) \quad i, j = 1, \dots, N_1, & a_{3,ij} &= a_3(\hat{\varphi}_j, \hat{\varphi}_i), \quad i, j = 1, \dots, N_2, \\
\tilde{a}_{2,ij} &= \left(c_0 + \frac{\alpha}{\lambda}\right) (\tilde{\varphi}_j, \tilde{\varphi}_i), & a_{2,ij} &= \Delta t a_2(\tilde{\varphi}_j, \tilde{\varphi}_i) \quad i, j = 1, \dots, N_3, \\
b_{1,ij} &= b_1(\varphi_j, \hat{\varphi}_i) \quad i = 1, \dots, N_2, \quad j = 1, \dots, N_1, & b_{2,ij} &= b_2(\tilde{\varphi}_j, \hat{\varphi}_i) \quad i = 1, \dots, N_2, \quad j = 1, \dots, N_3, \\
\tilde{a}_{4,ij} &= (\bar{\varphi}_j, \bar{\varphi}_i), & a_{4,ij} &= \Delta t a_4(\bar{\varphi}_j, \bar{\varphi}_i) \quad i, j = 1, \dots, N_4, \\
\tilde{a}_{5,ij} &= (\bar{\varphi}_j, \bar{\varphi}_i), & a_{5,ij} &= \Delta t a_5(\bar{\varphi}_j, \bar{\varphi}_i) \quad i, j = 1, \dots, N_4, & F_i &= \Delta t^2 F_{r^{n+1}}(\varphi_i) \quad i = 1, \dots, N_1, \\
G_i &= \Delta t G(\tilde{\varphi}_i) \quad i = 1, \dots, N_3, & J_{1,i} &= \Delta t J_{f_h^{n+1}}(\bar{\varphi}_i), & J_{2,i} &= \Delta t J_{f_h^{n+1}}(\bar{\varphi}_i) \quad i = 1, \dots, N_4,
\end{aligned}$$

and then, denoting

$$\mathbf{A} := \begin{bmatrix} \tilde{A}_1 + A_1 & \Delta t^2 B_1^T & \mathbf{O} & F \\ \mathbf{O} & \tilde{A}_2 + A_2 & -B_2^T & \mathbf{O} \\ B_1 & B_2 & -A_3 & \mathbf{O} \\ \mathbf{O} & \mathbf{O} & \mathbf{O} & \tilde{A}_4 + A_4 + \tilde{A}_5 + A_5 \end{bmatrix}, \quad \mathbf{X} := \begin{bmatrix} U_j \\ P_j \\ \Phi_j \\ (W_{1,j}, W_{2,j}) \end{bmatrix}$$

$$\mathbf{H} := \begin{bmatrix} 2\tilde{A}_1 U_j^n - \tilde{A}_1 U_j^{n-1} \\ G + \tilde{A}_2 P_j^n - B_2 \Phi_j^n \\ \mathbf{O} \\ J_1 + \tilde{A}_4 W_{1,j}^n + J_2 + \tilde{A}_5 W_{1,j}^n \end{bmatrix},$$

we deduce that the fully-discrete matrix problem for (4.6) reads

$$\mathbf{A} \mathbf{X}^{n+1} = \mathbf{H}^n,$$

which will be useful for the development of the numerical tests.

In addition, a Newton method with exact Jacobian is derived for the solution of (4.1)-(4.5) at each time step. Then, regarding both chemical species in a single vector \mathbf{W} , the tangent algebraic systems to be solved at each Newton step (for a given time step) adopt the following form

$$\begin{aligned}
\hat{A}_{11} \delta \mathbf{U}_{k+1}^s &+ \hat{B}_{13} \delta \mathbf{\Psi}_{k+1} &+ \hat{F}_1 \delta \mathbf{W}_{k+1} &= \mathbf{R}_{1,k}, \\
\hat{A}_{22} \delta \mathbf{P}_{k+1}^f &- \hat{B}_{23} \delta \mathbf{\Psi}_{k+1} & &= \mathbf{R}_{2,k}, \\
\hat{B}_{13}^T \delta \mathbf{U}_{k+1}^s &+ \hat{B}_{32} \delta \mathbf{P}_{k+1}^f &- \hat{A}_{33} \delta \mathbf{\Psi}_{k+1} &= \mathbf{R}_{3,k}, \\
\hat{C}_{42}^k \delta \mathbf{U}_{k+1}^s & &+ (\hat{J}_4 + \hat{C}_{41}^k + \hat{A}_{41}) \delta \mathbf{W}_{k+1} &= \mathbf{R}_{4,k},
\end{aligned}$$

where $\delta(\cdot)_{k+1}$ represent the vector of nodal values for the incremental unknowns that are premultiplied by the respective elementary matrices constructed with the bilinear forms in (4.6) or their linearisation; that is, the matrix \hat{F}_1 is induced by the linearisation of $F_{r_h^{n+1}}(\cdot)$, \hat{A}_{11} by $a_1(\cdot, \cdot) + \tilde{a}_1(\cdot, \cdot)$, \hat{B}_{13} and \hat{B}_{13}^T by $b_1(\cdot, \cdot)$, \hat{A}_{22} by $a_2(\cdot, \cdot) + \tilde{a}_2(\cdot, \cdot)$, \hat{B}_{23} by $b_2(\cdot, \delta_t(\cdot))$, \hat{B}_{32} by $b_2(\cdot, \cdot)$, \hat{A}_{33} by $a_3(\cdot, \cdot)$, \hat{J}_4 by the linearisation of $J_{f_h^{n+1}}(\cdot)$ and $J_{g_h^{n+1}}(\cdot)$, \hat{C}_{41}^k and \hat{C}_{42}^k by the linearisation of $c(\cdot, \cdot, \cdot)$ (see its definition in [49, eq. (2.7)]), and \hat{A}_{41} by $\tilde{a}_4(\cdot, \cdot) + a_4(\cdot, \cdot)$ and $\tilde{a}_5(\cdot, \cdot) + a_5(\cdot, \cdot)$. The right-hand side vectors $\mathbf{R}_{i,k}$ account for body forces, mass sources, entities at the previous time step, and residuals from the previous Newton iteration k . The system is solved by the GMRES Krylov solver with incomplete LU factorisation (ILUT) preconditioning. The stopping criterion on the nonlinear iterations is based on a weighted residual norm dropping below the fixed tolerance of $1 \cdot 10^{-6}$.

The implementation of all numerical routines has been carried out using the finite element library FEniCS [2].

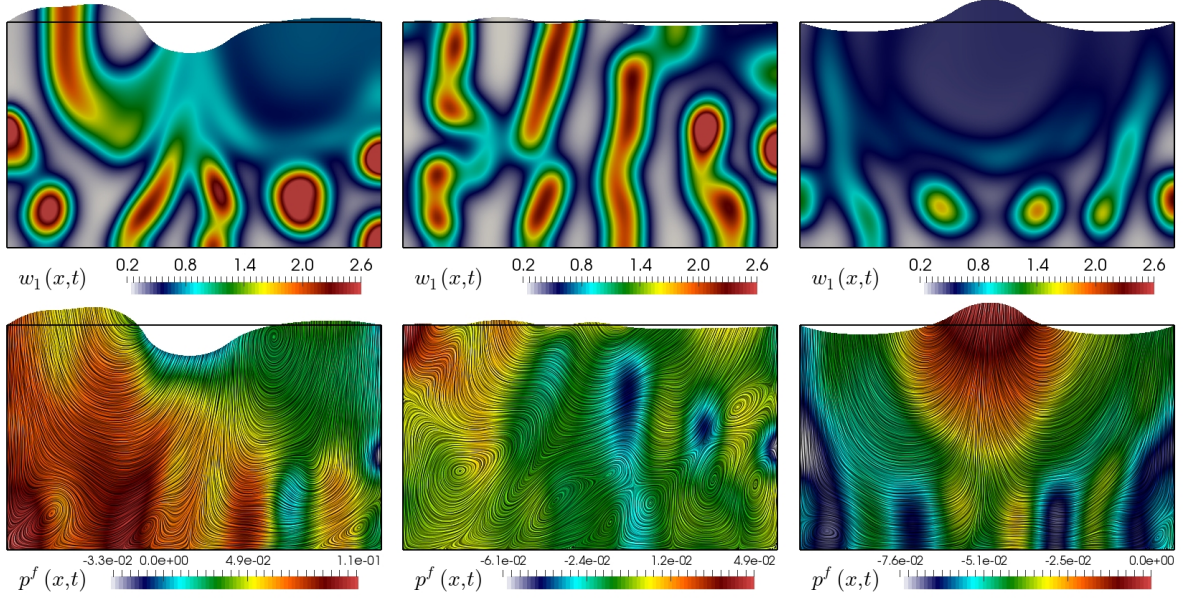


Figure 5.1: Test 1. Sample of concentrations of w_1 (top) and fluid pressure (bottom) at times $t = 0.5, 1, 1.75$ and plotted on the deformed domain according to the solid displacements.

5. Numerical tests

5.1. Test 1: Periodic traction preventing stable patterning

In order to investigate the impact that the structural deformation has on the emerging spatial patterns of solutes, we first consider the spatial domain $\Omega = (0, 1) \times (0, 0.6)$, where the clamped boundary is $\Gamma = \{\mathbf{x} : x_1 = 0, x_1 = 1, x_2 = 0\}$ and the top face constitutes Σ where we apply a periodic traction defined by

$$\mathbf{t} = \begin{cases} (0, -s_0 \sin(\pi t))^T & \text{if } 0.4 \leq x_1 \leq 0.6, \\ \mathbf{0} & \text{otherwise,} \end{cases}$$

with $s_0 = 25000$ (similarly as in the footing problem from e.g. [31]). According to (2.10)-(2.11), on Γ we also impose zero fluid pressure fluxes, whereas on Σ we set a uniform fluid pressure $p^f = 0$. The parameters that are modified with respect to Test 2 are only the coupling constants of active stress modulation $\tau = 100$ (using again $r = w_1 + w_2$), the direction $\mathbf{k} = (1, 0)^T$, the density $\rho = 1$, and the volume-dependent source $\gamma = 0.05$. The resulting patterns (exemplified by transients of the activator chemical w_1 and final states of poromechanical variables) are depicted in Figure 5.1. One can readily observe that, apart from altering substantially the distribution of chemical concentrations from the beginning of the simulation, the periodic traction applied on part of the top edge (and which only produces less than a 10% of vertical stretch) prevents the system from reaching a state with stable spatial patterns. For this test we have used a structured mesh.

5.2. Test 2: Small poromechanical effects

Next we take the domain as the disk centred at $(0.5, 0.5)$ with radius 0.5, and assume that the boundary coincides with Γ . Then the displacements are set to zero on the whole boundary and we take relatively small values for the coupling constants on the chemical source and on the active stress

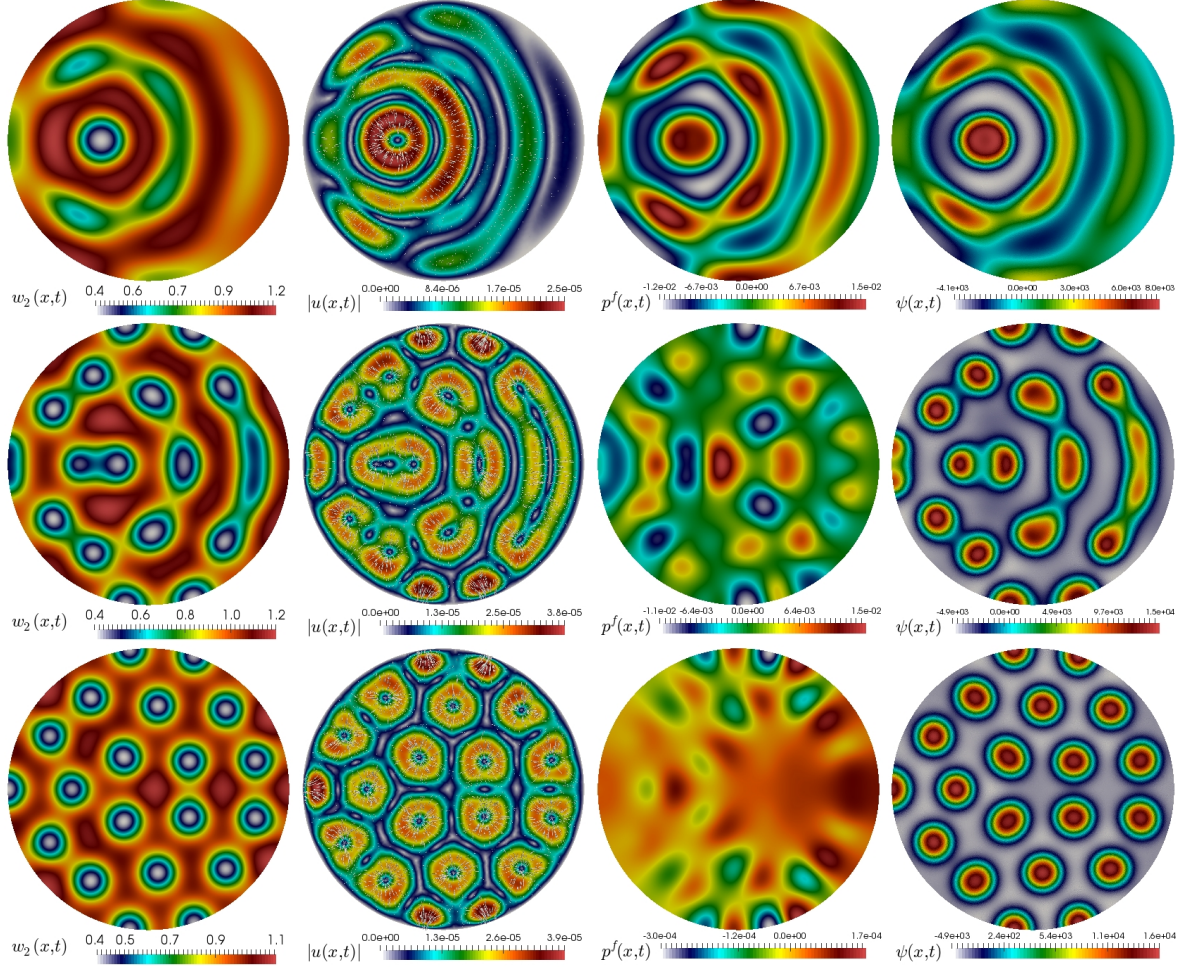


Figure 5.2: Test 2. Patterns generated with relatively small chemo-mechanical feedback $\gamma = 0.0001$ and clamped boundary conditions, plotted on the undeformed domain at times $t = 0.25$ (top), $t = 0.375$ (middle row), and $t = 1.5$ (bottom panels). From left to right: w_2 concentration, solid displacement magnitude, fluid pressure, and total pressure.

$\gamma = 0.0001$, $\tau = 100$, implying in particular that the patterns produced by the coupled poroelastic-advection-diffusion-reaction system are expected to be qualitatively similar to those observed on a fixed domain. In (2.8) we assume a dependence of the form $r = w_1 + w_2$, and the remaining model constants are taken as $D_1 = 0.05$, $D_2 = 1$, $\beta_1 = 170$, $\beta_2 = 0.1305$, $\beta_3 = 0.7695$, $E = 3 \cdot 10^4$, $\nu = 0.495$, $\rho = 1$, $c_0 = 1 \cdot 10^{-3}$, $\kappa = 1 \cdot 10^{-4}$, $\alpha = 0.1$, $\eta = 1$, $\mathbf{k} = (x_1 - 0.5, x_2 - 0.5)^T$. The initial condition for the chemicals is a perturbation of the homogeneous steady state $w_1^0 = \beta_2 + \beta_3$, $w_2^0 = \beta_3(\beta_2 + \beta_3)^{-2}$ and for the displacements and fluid pressure we use zero initial conditions. The domain is discretised into an unstructured mesh of 64926 triangles and we employ a fixed time-step $\Delta t = 0.0025$. The system is advanced until $t_{\text{final}} = 1.5$ and plots with patterns of w_2 , small deformations, as well as fluid and total pressures are shown in Figure 5.2. In the bottom row we can see how the initial perturbation of the steady state evolves into organised dot-shaped spatial structures, seen clearly for the inhibitor chemical w_2 and also captured by the total pressure. No deformation occurs along the domain boundary, but the local deformation patterns show also tissue contraction near the zones of high concentration of the activator species w_1 .

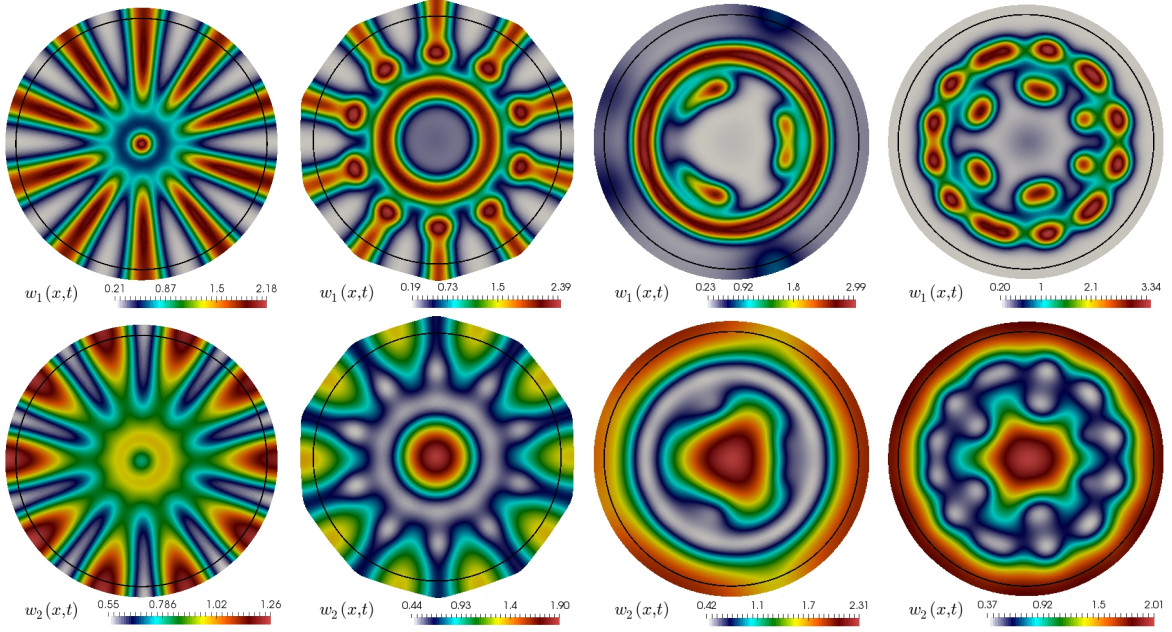


Figure 5.3: Test 3. Interplay between linear growth and active stress. Concentrations of w_1 and w_2 (top and bottom) on the deformed domain, at time $t = 1.25$, for different mild values of the coupling constants τ, τ_2 . The black circle in all plots represents the boundary of the initial domain.

5.3. Test 3: Linear growth and active stress

Maintaining the same domain and discretisation parameters as in Test 1 above, we now fix the mechano-chemical coupling constant $\gamma = 0.01$ and study the competing effect between linear growth with radial traction, and the active stress depending on the concentration of the activator species w_1 . This is done with an activation of the type $r = \tau_2 t + w_1^2$, and for this 2D case we consider Robin boundary conditions for the solid motion (2.9) with $\zeta = t\tau_2$, on the circular boundary (whereas for the 3D case below we impose zero normal displacement on the bottom of the cylinder and a traction $t = \tau_2 t n$ on the remainder of the boundary). We set k to be the radial vector, and vary τ, τ_2 . The results are shown in Figure 5.3. From left to right we display snapshots of the chemical patterns produced with the parameter choices $(\tau = 2 \cdot 10^5, \tau_2 = 0.2)$, $(\tau = 10^5, \tau_2 = 2)$, $(\tau = 10^4, \tau_2 = 10)$, and $(\tau = 100, \tau_2 = 20)$.

5.4. Test 4: Linear growth in 3D

We extend the previous test to assess the behaviour of the model and the finite element scheme in a 3D setting. We modify (2.8) to include axial symmetry on another preferential direction for active deformation. The domain is a cylinder of height 0.05 and radius 0.5, and we set

$$\sigma_{\text{act}} = -\tau [\tau_2 t k_{12} \otimes k_{12} + w_1^2 k_3 \otimes k_3],$$

where k_{12} is the radial vector in the plane $x_1 x_2$ and $k_3 = (0, 0, 1)^T$. This implies that the active deformation due to linear growth will occur in the radial direction whereas the stress due to the chemical concentration will act on the x_3 -direction. On the bottom surface we set zero normal displacements $u \cdot n = 0$ while on the remainder of the boundary we impose zero traction. In Figure 5.4 we show the resulting patterns of w_1 concentration for two sets of Lamé and poromechanical-chemical coupling parameters. For the first case we use $E = 1 \cdot 10^4$, $\nu = 0.499$, and $\tau = 10$, $\tau_2 = 20$, $\gamma = 0.05$ and show the patterns on the deformed domain in the left panels; while the plots on the right panels were produced

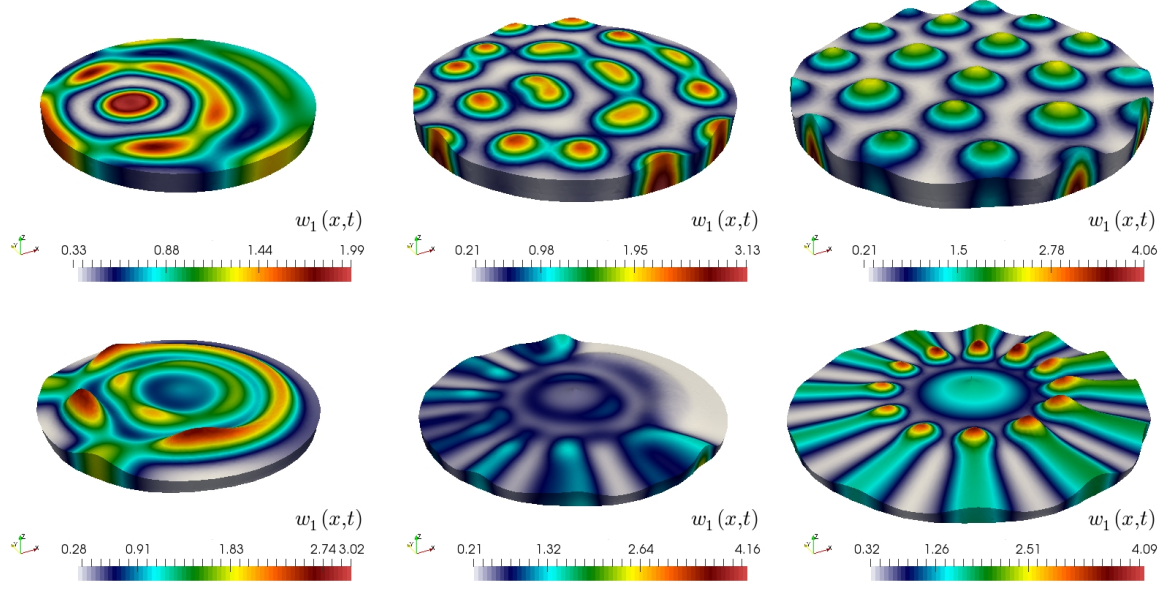


Figure 5.4: Test 4. Interplay between linear growth and active stress for two sets of elasticity and coupling parameters (top and bottom). Concentrations of w_1 on the deformed domain, at times $t = 0.25, 0.5, 1.25$ (left, centre, and right panels, respectively).

with $E = 1 \cdot 10^3$, $\nu = 0.3$, and $\tau = 50$, $\tau_2 = 60$, $\gamma = 0.1$. We observe stable pattern generation with the first set of model parameters, similar to the expected patterning in the case of pure reaction-diffusion effects, whereas the patterns on the right exhibit large qualitative differences in w_1 (also in the other species) as well as in the deformation behaviour.

5.5. Test 5: Application to the simulation of brain injuries and calcium propagation

We close this section with an example related to the one-way coupling between poroelastic deformations in the brain (induced by a localised high stress) and the subsequent propagation and reaction of two types of calcium concentration, intra-cellular and extra-cellular, throughout the tissue. This illustrative test is based on the kinetic and 1D models recently advanced in [21]. In there, the authors propose that hydrostatic stress build up due to the brain trauma affect (in an exponentially decreasing manner) the reacting fluxes between the calcium concentrations. We do not include acceleration but we propose to incorporate this in our model using a modification of (2.5)-(2.6) to include a dependence of the reaction terms on the total pressure

$$f(w_1, w_2, \psi) = -D_1(w_1 - w_2) + \frac{1}{\chi_1} \left[-\chi_1 + (1 + \chi_1) \exp(-k|\psi|) \right] \frac{w_2^2}{w_2^2 + k_1^2},$$

$$g(w_1, w_2, \psi) = -f(w_1, w_2, \psi) + D_2(w_0 - w_2) - \frac{1}{\chi_2} \left[-\chi_2 + (1 + \chi_2) \exp(-k|\psi|) \right] \frac{w_2}{w_2 + k_2},$$

where w_1, w_2 represent respectively, the extra-cellular and intra-cellular calcium concentrations (in [mM] units) and the model parameters are as in [21]

$$D_1 = 2.94 \cdot 10^{-6} [1/s], \quad D_2 = 3.17 \cdot 10^{-5} [1/s], \quad k_1 = 2 \cdot 10^{-4} [mM], \quad k_2 = 5 \cdot 10^{-4} [mM],$$

$$\chi_1 = 2 \cdot 10^3, \quad \chi_2 = 4 \cdot 10^3, \quad k = 4.5 \cdot 10^{-5} [Pa^{-1}], \quad w_0 = 0.1 [mM].$$

On the other hand, the fact that calcium activity effects are negligible in producing deformations of the poroelastic structure (at least, when compared to high stress impacts on the skull or with important

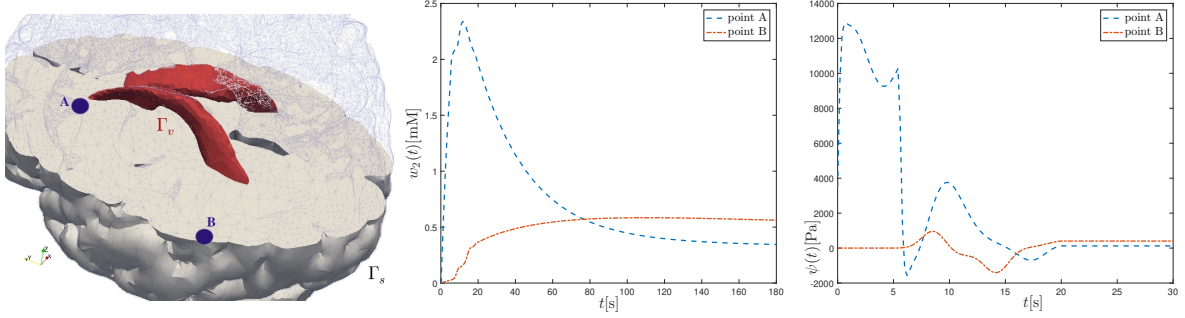


Figure 5.5: Test 5. Cut of the human brain geometry and tetrahedral mesh, showing boundaries on the ventricles Γ_v and near the skull Γ_s , also indicating points A and B where we record quantities of interest (left panel). Time evolution of intra-cellular calcium concentration and of total pressure (centre and right plots).

kinematic forces building up because of rapid shocks) implies that in our model the total stress (2.7) does not contain an active component modulated by w_1, w_2 . Also, our model is different than the one in [21] in that we do not consider viscoelastic effects but do include poroelasticity of the brain, and we also include diffusion of the calcium concentrations. The remaining constants in the model and the initial conditions adopt the values

$$E = 3.15 \cdot 10^4 \text{ [Pa]}, \quad \nu = 0.45, \quad \rho = 1130 \text{ [Kg/m}^3\text{]}, \quad \frac{\kappa}{\eta} = 10^{-5} \text{ [mm}^2\text{Pa}^{-1}\text{s}^{-1}\text{]}, \quad \alpha = 0.1, \\ c_0 = 3.9 \cdot 10^{-4} \text{ [Pa}^{-1}\text{]}, \quad \mathbf{u}^s(0) = \mathbf{0}, \quad p^f = 0, \quad \psi(0) = 0, \quad w_{1,0} = 1 \text{ [mM]}, \quad w_{2,0} = 10^{-4} \text{ [mM]}.$$

The spatial domain consists of a 3D structure of the human brain and the boundaries are split between ventricles and the outer meningeal region of the brain, in contact with the skull. The interstitial flow in this case is by cerebrospinal fluid. The domain consists of an adult human brain atlas [17, 23] and we use a tetrahedral mesh with 29037 vertices. An initial traction of magnitude $1.7 \cdot 10^4$ [Pa] is applied for 5.5 [ms] on a location near the ventricles and on the skull we impose zero normal displacements and zero fluid pressure, whereas on the ventricles we assume zero fluid pressure flux. We employ a timestep of $\Delta t = 0.1$ [ms] and run the simulation until $t = 180$ [s]. Transients of the intracellular calcium concentration as well as the total pressure are recorded on two points (one near the ventricles, point A, and another near the meninges, point B), and are displayed in Figure 5.5. One can observe an initial peak of several folds the initial homeostatic value of the intracellular calcium followed by a slowly decaying profile (which however does not goes back to the homeostatic value). We also see that the oscillations in total pressure due to the application of high stresses decrease over time. All this is qualitatively consistent with the model predictions from [21].

6. Concluding remarks

In this paper we have suggested a mathematical model to study the interaction between advecting reaction-diffusion dynamics within a poroelastic material. The set of equations assumes the regime of small strains and the tightly coupling mechanisms are primarily dependent on source functions of change of volume, and active stresses. This work represents an extension with respect to recent three-field models of poroelasticity using total pressure. We have demonstrated the feasibility of the model and of the numerical method to reproduce a variety of coupling scenarios including pattern suppression, linear growth instability, and other morphological changes. We are currently working towards including further details into the model. For example, the effects of chemotaxis and general cross-diffusion, as well as interfacial conditions for two-layered materials as encountered in [3, 14, 44]. Other

aspects to include in future directions are anisotropy of motion and of diffusion, more complicated geometries, and other coupling mechanisms such as stress-assisted diffusion [18].

Acknowledgements. The authors gratefully acknowledge the fruitful discussions with Jenny Dingwall, Aayush Kant, Belle Kim, and Tim Leach during the early stages of this work.

References

References

- [1] B. ALBERS, *Relaxation analysis and linear stability vs. adsorption in porous materials*. Cont. Mech. Thermo., 15(1) (2003) 73–95.
- [2] M.S. ALNÆS, J. BLECHTA, J. HAKE, A. JOHANSSON, B. KEHLET, A. LOGG, C. RICHARDSON, J. RING, M.E. ROGNES, AND G.N. WELLS, *The FEniCS project version 1.5*. Arch. Numer. Softw., 3(100) (2015) 9–23.
- [3] V. ANAYA, Z. DE WIJN, B. GOMEZ-VARGAS, D. MORA, AND R. RUIZ-BAIER, *Rotation-based mixed formulations for an elasticity-poroelasticity interface problem*. SIAM J. Sci. Comput., (2019) in press.
- [4] F. AREGA AND E. HAYTER, *Coupled consolidation and contaminant transport model for simulating migration of contaminants through the sediment and a cap*. Appl. Math. Model., 32 (2008) 2413–2428.
- [5] L. BERGER, R. BORDAS, K. BURROWES, V. GRAU, S. TAVENER, AND D. KAY, *A poroelastic model coupled to a fluid network with applications in lung modelling*. Int. J. Numer. Methods Biomed. Engrg., 32(1) (2016) e02731.
- [6] M.A. BIOT, *Theory of elasticity and consolidation for a porous anisotropic solid*. J. Appl. Phys., 26 (1955) 182–185.
- [7] M.K. BRUN, I. BERRE, J.M. NORDBOTTEN, AND F.A. RADU, *Upscaling of the coupling of hydromechanical and thermal processes in a quasi-static poroelastic medium*. Transp. Porous Media., 124(1) (2018) 137–158.
- [8] V.M. CALO, N.F. BRASHER, Y. BAZILEVS, AND T.J.R. HUGHES, *Multiphysics model for blood flow and drug transport with application to patient-specific coronary artery flow*. Comp. Mech., 43(1) (2008) 161–177.
- [9] A.J. CATLLÁ, A. MCNAMARA, AND C.M. TOPAZ, *Instabilities and patterns in coupled reaction-diffusion layers*. Phys. Rev. E., 85(2) (2012) 026215.
- [10] J. COLLIS, D.L. BROWN, M.E. HUBBARD, AND R.D. O’DEA, *Effective equations governing an active poroelastic medium*. Proc. R. Soc. A, 473 (2017) 20160755.
- [11] E.J. CRAMPIN, W.W. HACKBORN, AND P.K. MAINI, *Pattern Formation in Reaction-Diffusion Models with Nonuniform Domain Growth*. Bull. Math. Biol., 64(4) (2002) 747–769.
- [12] G.C. CRUYWAGEN, AND J.D. MURRAY, *On a tissue interaction model for skin pattern formation*. J. Nonlin. Sci., 2(2) (1992) 217–240.
- [13] I. DAVID, W. JUNCHENG, AND W. MATTHIAS, *Stability analysis of Turing patterns generated by the Schnakenberg model*. J. Math. Biol., 49(4) (2004) 358–390.

- [14] L.M. DE OLIVEIRA VILACA, M.C. MILINKOVITCH, AND R. RUIZ-BAIER, *Numerical approximation of a 3D mechanochemical interface model for skin patterning*. J. Comput. Phys., 384 (2019) 383–404.
- [15] L.M. DE OLIVEIRA VILACA, M.C. MILINKOVITCH, AND R. RUIZ-BAIER, *Coupling chemotaxis and poromechanics for the modelling of feather primordia patterning*. (2019), in preparation.
- [16] A.E. EHRET, K. BIRCHER, A. STRACUZZI, V. MARINA, M. ZÜNDEL, AND E. MAZZA, *Inverse poroelasticity as a fundamental mechanism in biomechanics and mechanobiology*. Nature Comm., 10 (2017) e1002.
- [17] Q. FANG AND D.A. BOAS, *Monte Carlo simulation of photon migration in 3D turbid media accelerated by graphics processing units*. Opt. Express 17(22) (2009) 20178–20190.
- [18] G.N. GATICA, B. GOMEZ-VARGAS AND R. RUIZ-BAIER, *Analysis and mixed-primal finite element discretisations for stress-assisted diffusion problems*. Comput. Methods Appl. Mech. Engrg., 337 (2018) 411–438.
- [19] A. GORIELY AND R. VANDIVER, *On the mechanical stability of growing arteries*. IMA J. App. Math., 75(4) (2010) 549–570.
- [20] G.W. JONES AND S.J. CHAPMAN, *Modeling growth in biological materials*. SIAM Rev., 54(1) (2012) 52–118.
- [21] A. KANT, T.K. BHANDAKKAR, N.V. MEDHEKAR, *Stress enhanced calcium kinetics in a neuron*. Biomech. Model. Mechanobiol., 17(1) (2018) 169–180.
- [22] J.J. LEE, K.-A. MARDAL, AND R. WINTHER, *Parameter-robust discretization and preconditioning of Biot’s consolidation model*. SIAM J. Sci. Comp., 39 (2017) A1–A24.
- [23] J.J. LEE, E. PIERSANTI, K.-A. MARDAL, AND M. ROGNES, *A mixed finite element method for nearly incompressible multiple-network poroelasticity*. SIAM J. Sci. Comp., 41(2) (2019) A722–A747.
- [24] P. LIU, J. SHI, Y. WANG, AND X. FENG, *Bifurcation analysis of reaction-diffusion Schnakenberg model*. J. Math. Chem., 51 (2013) 2001–2019.
- [25] R.T. MAUCK, C.T. HUNG, AND G.A. ATESHIAN, *Modelling of neutral solute transport in a dynamically loaded porous permeable gel: implications for articular cartilage biosynthesis and tissue engineering*. J. Biomech. Engrg., 125 (2003) 602–614.
- [26] E. MOEENDARBARY, L. VALON, M. FRITZSCHE, A.R. HARRIS, D.A. MOULDING, A.J. THRASHER, E. STRIDE, L. MAHADEVAN, AND G.T. CHARRAS, *The cytoplasm of living cells behaves as a poroelastic material*. Nature Materials., 12 (2013) 3517.
- [27] P. MOREO, E.A. GAFFNEY, J.M. GARCÍA-AZNAR, AND M. DOBLARÉ, *On the modelling of biological patterns with mechanochemical models: Insights from analysis and computation*. Bull. Math. Biol., 72(2) (2010) 400 – 431.
- [28] J.D. MURRAY AND G.F. OSTER, *Generation of biological pattern and form*. Math. Med. Biol., 1(1) (1984) 51 – 75.
- [29] L. MURPHY AND A. MADZVAMUSE, *A moving grid finite element method applied to a mechanobiochemical model for 3D cell migration*. Submitted preprint (2019). Available from <https://arxiv.org/abs/1903.09535>.
- [30] A.A. NEVILLE, P.C. MATTHEWS, AND H.M. BYRNE, *Interactions between pattern formation and domain growth*. Bull. Math. Biol., 68(8) (2006) 1975–2003.

- [31] R. OYARZÚA AND R. RUIZ-BAIER, *Locking-free finite element methods for poroelasticity*. SIAM J. Numer. Anal., 54(5) (2016) 2951–2973.
- [32] R. PENTA, D. AMBROSI, AND R.J. SHIPLEY, *Effective governing equations for poroelastic growing media*. Q. J. Mech. Appl. Math., 67 (2014) 69–91.
- [33] G.P. PETERS AND D.W. SMITH, *Solute transport through a deforming porous medium*. Int. J. Numer. Analytical Methods Geomech., 26 (2002) 683–717.
- [34] M. POURJAFAR AND K. SADEGHY, *Pressure-driven flows of Quemada fluids in a channel lined with a poroelastic layer: A linear stability analysis*. J. Non-Newt. F. Mech., 242 (2017) 23 – 47.
- [35] M. RADSZUWEIT, S. ALONSO, H. ENGEL, AND M. BÄR, *Intracellular mechanochemical waves in an active poroelastic model*. Phys. Rev. Lett., 110(13) (2013) 138102.
- [36] M. RADSZUWEIT, H. ENGEL, AND M. BÄR, *An active poroelastic model for mechanochemical patterns in protoplasmic droplets of physarum polycephalum*. PLOS ONE, 9(6) (2014) e99220.
- [37] P. RECHO, A. HALLOU, AND E. HANNEZO, *Theory of mechano-chemical patterning in biphasic biological tissues*. PNAS., 116(12) (2019) 5344–5349.
- [38] R.F. REIS, R. WEBER DOS SANTOS, B.M. ROCHA, AND M. LOBOSCO, *On the mathematical modeling of inflammatory edema formation*. Comput. Math. Appl., (2019) in press.
- [39] E.J. ROUTH, *A Treatise on the Stability of a Given State of Motion: Particularly Steady Motion*. Macmillan and Company, 1877. ISBN 02013331.
- [40] P. ROYER AND F. CHERBLANC, *Homogenisation of advective-diffusive transport in poroelastic media*. Mech. Res. Commun., 37(2) (2010) 133–136.
- [41] R. SACCO, P. CAUSIN, C. LELLI, AND M.T. RAIMONDI, *A poroelastic mixture model of mechanobiological processes in biomass growth: theory and application to tissue engineering*. Meccanica, 52(14) (2017) 3273–3297.
- [42] J. SCHNAKENBERG, *Simple chemical reaction systems with limit cycle behaviour*. J. Theoret. Biol., 81(3) (1979) 389–400.
- [43] R. SEYDEL, *Practical Bifurcation and Stability Analysis*. Inter. App. Math. Springer, New York (2009).
- [44] R.E. SHOWALTER, *Diffusion in poro-elastic media*. J. Math. Anal. Appl., 251 (2000) 310–340.
- [45] K.H. STØVERUD, M. ALNÆS, H.P. LANGTANGEN, V. HAUGHTON, AND K.-A. MARDAL, *Poro-elastic modeling of Syringomyelia – a systematic study of the effects of pia mater, central canal, median fissure, white and gray matter on pressure wave propagation and fluid movement within the cervical spinal cord*. Comput. Methods Biomech. Biomed. Engrg., 19(6) (2016) 686–698.
- [46] L.A. TABER, *Biomechanics of growth, remodeling, and morphogenesis*. Appl. Mech. Rev., 48 (1995) 487–545.
- [47] K. TERZAGHI, *Theoretical Soil Mechanics*. Wiley, New York (1943).
- [48] J.C. VARDAKIS, D. CHOU, B.J. TULLY, C.C. HUNG, T.H. LEE, P.-H. TSUI, AND Y. VENTIKOS, *Investigating cerebral oedema using poroelasticity*. Med. Engrg. Phys., 38 (2016) 48–57.
- [49] N. VERMA, B. GÓMEZ-VARGAS, L.M. DE OLIVEIRA VILACA, S. KUMAR, AND R. RUIZ-BAIER, *Well-posedness and discrete analysis for advection-diffusion-reaction in poroelastic media*. Submitted preprint (2019). Available from arxiv.org/abs/1908.09778.

- [50] S. ZAK, *Modern automatic control*. Lecture notes, University of Purdue, 2015.
- [51] A.M. ZÖLLNER, A. B. TEPOLE, A.K. GOSAIN, AND E. KUHL, *Growing skin: tissue expansion in pediatric forehead reconstruction*. Biomech. Model. Mechanobiol., 11(6) (2012) 855–867.